CDF/ANAL/ELECTROWEAK/CDFR/1245

Lepton Charge Asymmetry from W -> μ ν at the Tevatron Collider.

Sandra Leone

INFN and University of Pisa, Italy

Thesis submitted to the University of Pisa in June 1990.

Advisors Profs Giorgio Belettini and Hans Grassmann.

Table of contents

Introduction

This work has been done within the CDF (Collider Detector at Fermilab) Collaboration, which is an international collaboration among teams of the United States, Italy and Japan. The CDF detector is a multipurpose detector, built to study proton-antiproton interactions at the Fermilab Tevatron Collider. The Fermilab Tevatron Collider provides a center of mass energy of 1.8 TeV, the highest energy available in the world. During its first high luminosity run in 1988-89, CDF collected a data sample of integrated luminosity 4.4 pb^{-1}.

Among many other interesting data samples, the run yielded about 4000 W's decaying to an electron or muon and a neutrino. The high quality of this sample enabled CDF to make measurements of several W parameters.

This thesis presents a study of the W production mechanism. At the high energy of the Tevatron, W's are produced at very low x (x is the momentum fraction relative to the beam momentum). The W rapidity distribution can be used to measure the momentum distribution of the incoming partons. Different sets of parton distribution functions have been proposed in the past. They were all based on data measured at low energy, in deep-inelastic lepton scattering experiments. When evolved to $\sqrt{s}$ = 1.8 TeV, they differ quite substantially at x=0. In our experiment, using different sets of structure functions, one predicts different W rapidity distributions. Consequently, studying the W rapidity distributions becomes a new way to test parton distribution functions at about x=0.05. Also, since W are created at first order by a u - d interaction, one is sensitive to the u / d ratio.

These investigations are interesting in their own right . In addition, the understanding of the parton distribution functions will be important for future measurements, such as an accurate W mass measurement and a measurement of the ratio $R = \sigma(W) / \sigma(Z)$.

Because of the large fluctuations in longitudinal momentum of particles escaping through the forward/backward detector holes, the longitudinal momentum of neutrinos and therefore of W's cannot be measured. At the SPS collider this problem could be solved by imposing the value of the W mass to the charged lepton-missing momentum system. When doing this, one gets 2 solutions for the neutrino four-momentum. At $\sqrt{s}$ = 630 GeV, based on Montecarlo studies one found that the solution giving the smaller W longitudinal momentum was the right one in most cases. Therefore one could reconstruct the W four-momentum with a high efficiency. At the Tevatron, the W's have a large longitudinal boost and one finds that the same method will not work. However, the W rapidity distribution has a strong influence on the rapidity distribution of the decay leptons. We therefore studied the charged lepton rapidity distribution and derived from it information on the underlying proton structure functions.

The W's decay according to the V - A coupling. The lepton rapidity distribution is also influenced by this electro-weak mechanism of decay. Still, since this effect can be accounted for very accurately, the lepton rapidity distribution carries information on the u and d quark x distributions inside the proton.

As an indicator of the lepton rapidity distribution we study the asymmetry parameter, defined as follows:

$$A(\eta) = \frac{N^+(\eta) - N^-(\eta)}{N^+(\eta) + N^-(\eta)}$$

where N^+ = number of events at q(q=lepton charge) x η(η=lepton pseudorapidity)>0. Accordingly N^- corresponds to $q \times \eta < 0$. If we assume, as we have tested in many studies, that our lepton detection efficiency at a given rapidity is charge independent, the asymmetry function is detector independent. A comparison between data and theoretical predictions is then straighforward.

Possible systematic problems of the detector could influence the measured asymmetry. We have studied the systematics and we have determinated that these errors are very small. At present the precision of our measurement is limited by the statistical uncertainty. However, the available statistics is sufficient to observe that some parton structure functions are unfavoured. The results obtained in the muon and in the electron channel are in good agreement with each other. Present CDF plans call for the collection of 20 pb^{-1} of data for the 1991 run. This will allow an improved measurement of the lepton charge asymmetry. The detector will also be improved and muons and electrons are expected to be detected with a high efficiency also at larger values of pseudorapidity. This will allow the asymmetry measurement to be extended to higher values of pseudorapidity.

This thesis is organized as follows:
Chapter I contains a short summary of the theoretical background relative to this work starting from the Standard Model and then describing the mechanism of W production at ppbar colliders. Chapter II describes briefly the Tevatron Collider and the CDF experiment, paying particular attention to those parts of the detector which play a major role in this analysis: Central Tracking System, Central Calorimeters, Central Muon Chambers and the Trigger. The subject of Chapter III is the simulation of W events done using the Papageno Montecarlo, the study of the Asymmetry and the effect of higher order corrections ($Pt(W) \neq 0$) expected from Montecarlo. In Chapter IV, the data analysis is discussed. Muon data processing, muon identification, muon quality cuts, W event selection and estimate of the possible backgrounds are presented. Chapter V describes the efficiency studies. Finally Chapter VI reports the results of the analysis both in the muon and in the electron channel and discusses the possible future improvements.

Chapter I

Theoretical frame

1.1 The Standard Model and QCD

The existing picture of the fundamental constituents of matter and their interactions is currently summarized in a theoretical framework known as the "Standard Model". All matter appears to be composed by quarks and leptons, which are pointlike, structureless, spin-1/2 particles.[1] Leaving aside gravitation, the interactions among these particles are of three types: weak, electromagnetic and strong. These interactions are described by gauge theories and are mediated by spin-1 gauge bosons. The quarks participate in all three interactions, while the leptons only in the weak and electromagnetic ones. The fundamental particles can be grouped in doublets of three families:

$$\begin{matrix} \nu_e & \nu_\mu & \nu_\tau \\ e & \mu & \tau \end{matrix}$$

and

$$\begin{matrix} u & c & [t] \\ d & s & b \end{matrix}$$

Symmetry considerations and the need for cancellations of infinities in the theoretical predictions of a number of observables suggest the existence of a sixth quark of charge +2/3 named "top" which has not yet been discovered. The current experimental lower limit on the top mass comes from CDF and is $M_{top} > 89$ GeV/ c^2 [2].

Electromagnetic interactions are described by the Quantum Electro-Dynamics (QED). QED is based on a U(1) symmetry. The conserved quantity related to the symmetry is the electric charge. Electromagnetic interactions are mediated by massless photons coupled to the electric charge.

Weak interactions are mediated by massive bosons ($W^{\pm}, Z^o$). Glashow, Salam and Weinberg in 1967 suggested to incorporate the laws of electromagnetism and weak interactions in one unified model, the "Electroweak" model. This is based on a non-abelian, spontaneously broken symmetry SU(2) x U(1). The conserved charges associated with this symmetry are the weak isospin and the hypercharge. The breaking of the symmetry causes the W and Z bosons to become massive. In the Standard Model the mass of the charged intermediate boson is given to lowest order by:

$$M_W^2 = \frac{\pi\alpha}{G_F\sqrt{2}x_W(1 - \Delta r)} = \frac{(37.3 \text{ GeV}/c^2)^2}{x_W(1 - \Delta r)}$$

where $x_W = \sin^2 \theta_W$ contains the weak mixing angle and $(1 - \Delta r)$ accounts for radiative corrections (hadron loops) and depends on the unknown top quark mass. The last measured value at CDF is $M_W = 79.83 \pm 0.44$ GeV/c^2 [3].

The theory of strong interactions is the Quantum Chromodynamics (QCD). QCD is based on a non-abelian exact gauge symmetry SU(3). Strong interactions are mediated by neutral massless gauge bosons called gluons, coupled to a conserved charge called colour. The coupling constant of strong interactions, α_s, can be expressed in

terms of the relative distance, or, equivalently, of the four momentum Q^2 transferred between colour states. The scale of the strong interaction in momentum space is determined by a constant called Λ. The value of Λ is not predicted by QCD. It is a free parameter to be derived from experiment. As the Q^2 of the interaction increases, the coupling constant α_s decreases until the quarks and gluons are only weakly interacting with each other[4].

The degree of experimental support for the electroweak theory and QCD is rather different. For the electroweak theory the goal at the present is to make precise quantitative tests of detailed predictions, while in the case of QCD many comparisons between theory and experiment are still at the qualitative level, either because precise theoretical predictions have not yet been worked out, or because of difficulties with the required measurements. The work reported in this thesis gives a method to test some QCD predictions, by measuring quantities related only to weakly interacting particles.

1.2 Parton Model and Structure functions.

Nucleons contain three valence quarks. However, according to the uncertainty relation, the three valence quarks could be joined for a short duration by quark-antiquark pairs. Such pairs form the so-called quark-antiquark sea. In addition, gluons are also present in the nucleon. We nowadays assume that the proton consists of partons, which are quarks, antiquarks and gluons. Partons behave like free and independent particles on a scale which is small compared to the size of the proton [5]. The partons inside a proton of momentum p^μ carry momenta $x_j p^\mu$, where the momentum fraction x_j satisfys the rules:

$$0 < x_j < 1 \quad \text{and} \quad \sum_{\text{parton } j} x_j = 1$$

Each parton is distributed in x_j according to some probability function.

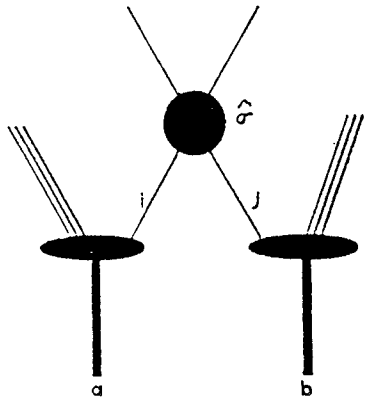

Fig. 1.1 Parton Model representation of a parton-parton hard reaction.

Our knowledge of the proton structure is mostly based on deep inelastic scattering experiments of high energy leptons on nucleon targets. These experiments measured some parton distribution functions.
Consider for example the case of a charged lepton scattering on a proton target. The simplest description of the collision between the high energy charged lepton and a parton inside the proton as the interaction between two pointlike particles, predicts distribution functions which depend only on x and not on Q^2, which is the squared mass of the

exchanged virtual boson. Since x is dimensionless, there is no relevant scale of mass or lenght in the process (scale invariance,[1]). However, deep inelastic scattering data showed red-shifting variations in the distribution functions, at fixed x, with increasing Q^2. This scaling invariance violation is now interpreted as being due to gluon radiation of the initial state, whose importance increases with Q^2.

It is convenient to parametrize the parton distributions with a limited number of different functions of x and Q^2. The proton contains:

- up quark : $u_v(x, Q^2) + u_s(x, Q^2)$ (valence plus sea)
- down quark : $d_v(x, Q^2) + d_s(x, Q^2)$ (valence plus sea)
- up antiquark : $u_s(x, Q^2)$ (sea only)
- down antiquark : $d_s(x, Q^2)$ (sea only)
- strange,charm,bottom and top quarks and antiquarks : $q_s(x, Q^2)$ (sea only)
- gluons : $G(x, Q^2)$

The flavor quantum numbers of the proton are carried by the valence quarks. The distributions are normalized as:

$$\int_0^1 dx u_v(x,Q^2) = 2$$

$$\int_0^1 dx d_v(x,Q^2) = 1$$

The parton distributions are also overall constrained by the momentum sum rule :

$$\int_0^1 dx\, X\, [\, u_v+d_v+G+2(u_s+d_s+s_s+c_s+b_s+t_s)] = 1$$

Multiplying the parton distribution functions by the fractional momentum x, we obtain the parton structure functions. Structure functions cannot be obtained theoretically in QCD, but rather are extracted from experimental data. Data cover, of course, a finite range of Q^2. At finite x, evolution to higher Q^2 is then predicted by the Altarelli-Parisi equations (1977).

Different sets of structure functions have been proposed in the past. The various parametrizations available in the literature were, in general, derived from fits to different combinations of deep inelastic data, and evolved after assuming different values of Λ. Information on the gluon structure function is considerably harder to obtain than for quarks. This is because DIS experiments use weak and electromagnetic probes which do not couple directly to gluons. One must rely on rather indirect methods for its determination. A source of uncertainty in the result is associated, in particular, with the correlation between the adopted parameter scale Λ and the derived shape of the gluon distribution. A softer gluon distribution results if a smaller value of Λ is chosen. Arbitrarily changing Λ independently of the gluon distribution can give rise to very misleading results and potentially unreliable predictions. Deriving the structure functions to be used to predict hard hadrons cross-sections from deep inelastic scattering data is a questionable method. For example DIS hardly cover the region of small x ($0.02 < x < 0.12$) which are probed at the Fermilab Tevatron Collider for the W production, so structure functions are poorly known at these x-values. Furthermore, deep inelastic data require comparison of results from different targets and apparata,

implying the presence of different systematic uncertainties. On the other hand, we hope that our work will eventually allow to derive our own structure functions, to be directly applicable to most hard processes studied at CDF.

We will compare our results to the following sets of structure functions. Eichten-Hinchliffe-Lane and Quigg (EHLQ, [6]) and Duke and Owens (DO, [7]) evaluated their sets of structure functions based on experimental data available up to the early 1980's, and using lowest order QCD evolution. As an example, in figures 1.2 we show the parton distributions for two sets of Eichten structure functions, obtained considering two different values of Λ.

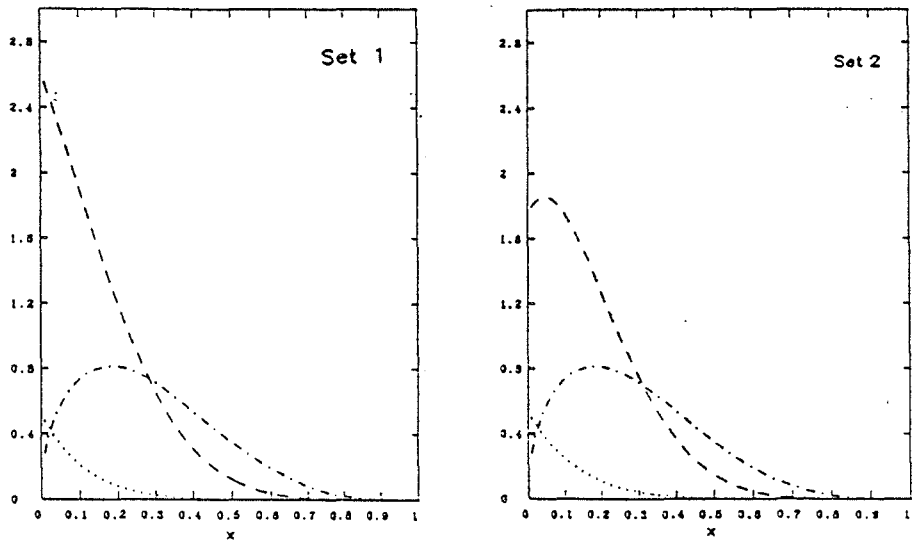

Fig. 1.2 Parton distributions of Set 1 (Λ = 200 MeV) and Set 2 (Λ = 290 MeV) Eichten structure functions at Q^2 = 5 GeV^2. The dashed line corresponds to the gluon (x G(x)), the dashed-dotted line to the valence quarks (x [$u_v + d_v$]) and the dotted line to the sea quarks (x [$u_s + d_s + 2s_s$]) [6].

Martin-Roberts and Stirling (MRS,[8]) evaluated three sets of structure functions, characterized by different gluon distributions. They included next-to-leading order
corrections and fit a wide range of newer experimental data. Also Diemoz-Ferroni-Longo and Martinelli (DFLM,[9]) used next-to-leading order calculations to obtain their sets of structure functions. The accuracy with which these distributions can be determined has important implications in measuring several Standard Model parameters. For example, one of the systematic uncertainties on the measurement of the W mass comes from the choice of the parton distribution functions [3].

1.3 W production at $p\bar{p}$ colliders

In lowest order, at $p\bar{p}$ colliders the W's are produced by a quark-antiquark annihilation. High order corrections involve gluon radiation from the incoming quarks and gluon-quark scattering. The cross section corresponding to the elementary reaction producing W's is given by :

$$\sigma_{p\bar{p}\to W} = \sum_{i,j} \int dx_1 dx_2 f_i(x_1) f_j(x_2) \hat{\sigma}_{i+j\to W}(\hat{s})\, \delta (s x_1 x_2 - \hat{s})$$

where $f_i (x_1)$ is the parton probability distribution, i.e. the probability of finding a parton of species i inside the proton carrying a fraction x_1 of the proton momentum,

$\hat{s} = s\, x_1\, x_2$ is the cms energy squared of the parton interaction and $\hat{\sigma}_{i+j\to W}$ is the W production cross section at parton level. The parton momentum fractions satisfy the requirements:

$$x_a\, x_b = \frac{M_W^2}{s}$$
$$x_a - x_b = X_W$$

where M_W is the mass of the W and X_W is its momentum fraction.

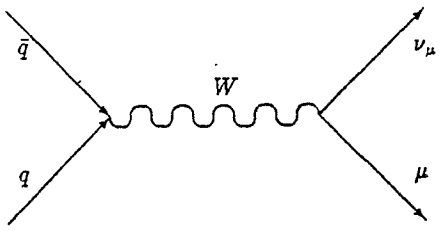

Fig. 1.3 Drell-Yan production of W boson.

When $\sqrt{s}$ is increased from the SPS to the Tevatron by a factor of 3, the average value of x in W production shifts from about 0.15 at CERN $p\bar{p}$ collider energies to about 0.05 at the Tevatron, i.e. from a regime where the valence-valence quark reactions dominate to a regime where the sea quarks become increasingly important and the valence-sea quarks reactions are the dominant sources of weak bosons. Fig. 1.4 shows the W production cross section in $p\bar{p}$ collision as a function of $\sqrt{s}$. The separate contributions from valence-valence, valence-sea and sea-sea quark interactions are also shown (obtained using the MRS1 structure function). At the Tevatron the charm quark-sea reaction $c\,\bar{s} \to W^+$ becomes more relevant. The charm quark is expected to contribute to about one percent to the total W-boson cross section at $\sqrt{s}$ = 630 GeV and about four percent at the Tevatron energy $\sqrt{s}$ = 1.8 GeV [10].

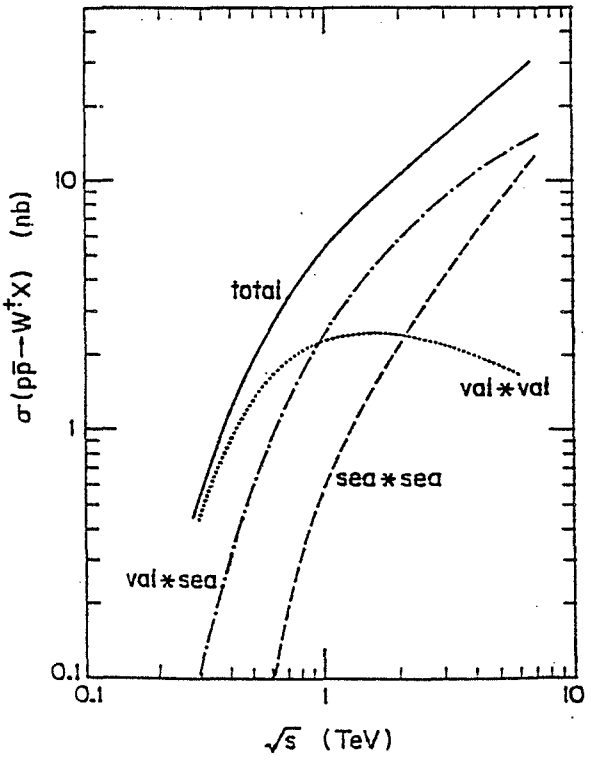

Fig. 1.4 W production cross-section in $p\bar{p}$ collisions as a function of $\sqrt{s}$ (MRS1) [10].

1.4 Asymmetry in W --> l ν decay.

1.4.1 The Rapidity variable.

In high-energy collisions the longitudinal momentum distribution is often discussed in terms of the rapidity variable:

$$y = \frac{1}{2} \ln\left(\frac{E + P_{\parallel}}{E - P_{\parallel}}\right)$$

where E is the particle energy and $P_{\parallel}$ is the longitudinal component of the particle momentum. If a Lorentz transformation is made to another frame, moving at velocity β along the z-axis (incident beam direction) the particle rapidity in the new frame is given by:

$$y' = y + \frac{1}{2} \ln\left(\frac{1 - \beta}{1 + \beta}\right)$$

This means that the y distribution is invariant under Lorentz transformation, which simply amounts to a shift of the origin in y. The rapidity is an additive quantity, like the velocity at non relativistic energy. In case of massless particles,
or when the particle transverse momentum is much larger than the particle mass and at angles not too small, it is useful to approximate y with the pseudorapidity variable, which depends only on the particle polar angle:

$$\eta = \frac{1}{2} \ln\left(\frac{1 + \cos\theta}{1 - \cos\theta}\right) = - \ln\left(\mathrm{tg}\frac{\theta}{2}\right)$$

where θ is the angle between the momentum of the outgoing particle and the proton momentum.

1.4.2 W rapidity distribution at production.

The distributions of partons which are responsible for the production of weak bosons can be investigated by the study of the rapidity distribution of the produced W bosons. In this way, many systematic uncertainties present in deep-inelastic data are eliminated. About 85 % of the W particles are created by a valence - sea or a valence - valence quark interaction. In those reactions, where at least one valence-quark is involved, a u quark in the proton strikes a $\bar{d}$ quark in the antiproton, if a W^+ particle is created.

The u and d quark momentum distributions are not identical. The u quark tends to carry a higher fraction of the proton momentum. Therefore, W^+ are produced preferentially boosted in the proton beam direction and W^- in the opposite direction. In fig. 1.5 we show the predicted W^+ rapidity distribution. We see that different choices of structure functions give different results (note the log scale).

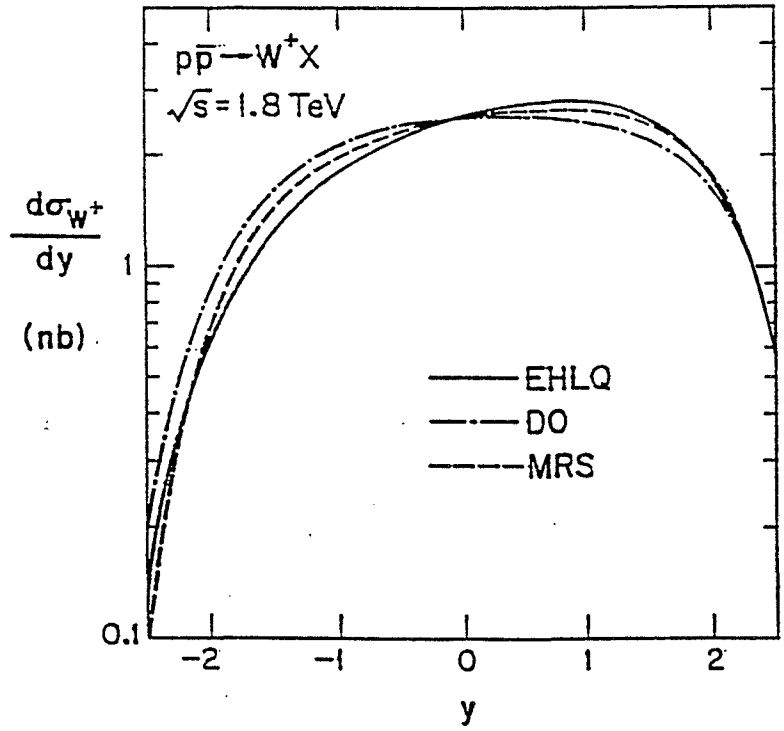

Fig. 1.5 Rapidity distribution of W^+ production at the Tevatron, based on the parton densities of EHLQ1, DO1 and MRS1 [10].

As we can deduce from fig. 1.6, this uncertainty is associated with a different x-dependence of the ratio of the valence up-quark to the valence down-quark densities in a proton.

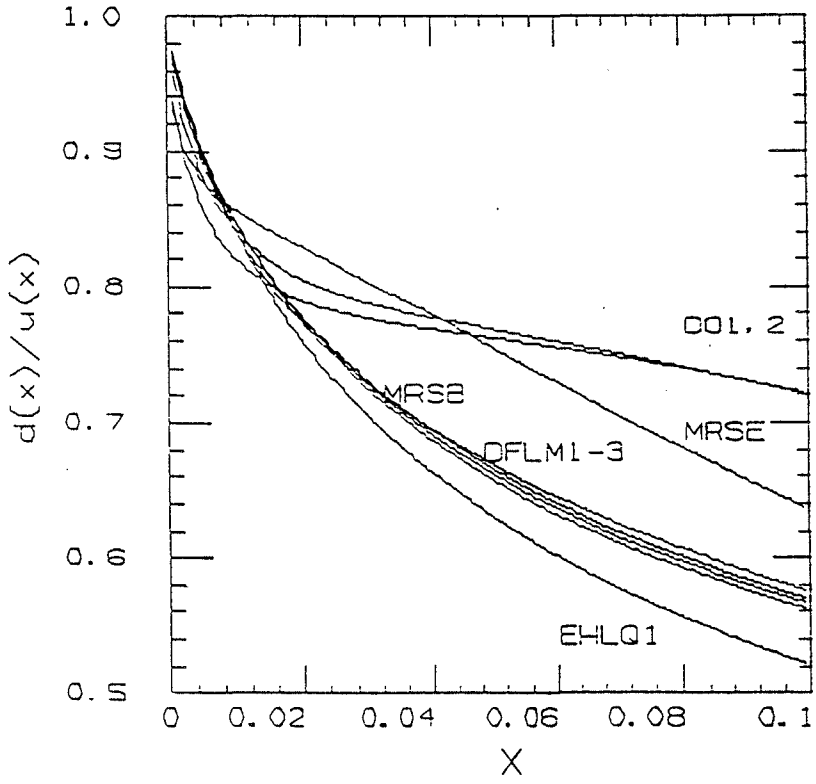

Fig. 1.6 The ratio d(x)/u(x) in the range $x < 0.1$ for $Q^2 = M_W{}^2$, for a number of different structure functions [14].

We can define the asymmetry in the W rapidity distribution as:

$$A_{W^+}(\sqrt{s}, y) = A_{W^-}(\sqrt{s}, -y) = \frac{\sigma_{W^+}(\sqrt{s}, y) - \sigma_{W^+}(\sqrt{s}, -y)}{\sigma_{W^+}(\sqrt{s}, y) + \sigma_{W^+}(\sqrt{s}, -y)}$$

where $\sigma_{W^+} = \frac{d\sigma}{dy}(p\bar{p} \rightarrow W^+X)$ (fig. 1.7). The differences among the predicted curves may be used to estimate the statistical precision needed to fix the appropriate parametrization of $u(x)/d(x)$ at collider energies.

The features of this asymmetry function and its relationship with the proton structure have been largely discussed in publications (see refs. 10 and 11). Considering that this is not the main subject of our study, we only remind, from reference 11, that it is possible to express the ratio $F_2^n(x)/F_2^p(x)$ in terms of the proton quark densities as:

$$\frac{F_2^n}{F_2^p}(x, Q^2=Q^2_{DIS}) \approx \frac{F_2^n}{F_2^p}(x, Q^2=M^2_W) = \frac{u + 4d + 7S}{4u + d + 7S}$$

where the functions $F_2^n(x)$ and $F_2^p(x)$ are the form factors measured in DIS neutrino experiments. A SU(3) flavor-symmetric sea is assumed (S = sea).

Given the above relationship, one finds numerically that the W production asymmetry can be related to the DIS form-factors by the approximate relation:

$$A_{W^+} \approx 1.2\{ \frac{F_2^n}{F_2^p}(x_2) - \frac{F_2^n}{F_2^p}(x_1) \}$$

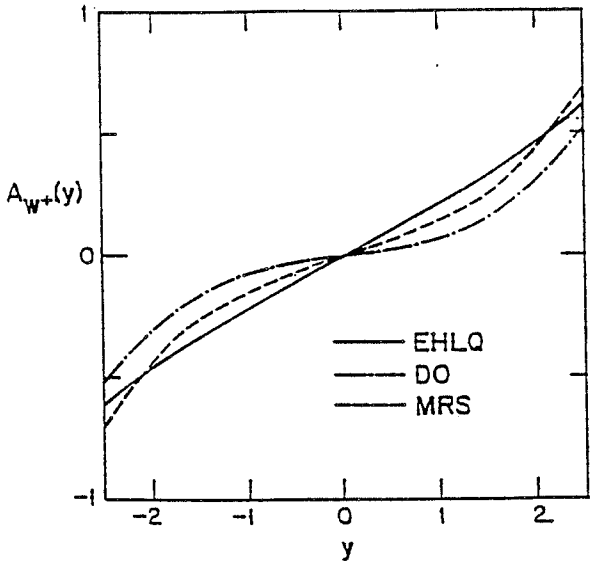

Fig. 1.7 Asymmetry A(y) of the rapidity distribution for W^+ at production at the Tevatron [10].

1.4.3 Leptonic W decay.

Up to now, practically the only way to experimentally observe W's is the lepton decay channel:

$$W^{\pm} \rightarrow l^{\pm} \nu$$

Combining the leptons four-momentum vectors, one would get the W four-momentum and its rapidity. But we cannot measure the longitudinal component of the neutrino momentum. So we do not observe directly the longitudinal momentum of the W's. One attempt to overcome this difficulty is to impose the mass of the W on the lepton-neutrino system. This will yield two solutions for the longitudinal component of the neutrino momentum, one corresponding to the neutrino being emitted forwards in the W rest frame, the other corresponding to the neutrino being emitted backwards. The two solutions for the neutrino longitudinal momentum $P_{||}^{\nu}$ are given by:

$$P_{||}^{\nu}=\frac{P_{||}^{\mu}(M_W^2+2P_t^{\mu}P_t^{\nu}\cos\phi)\pm P_{\mu}\sqrt{(M_W^2+2P_t^{\mu}P_t^{\nu}\cos\phi)^2-4P_t^{\mu^2}P_t^{\nu^2}}}{2P_t^{\mu^2}}$$

where P_t denotes the transverse momentum, ϕ is the angle between the muon and the neutrino transverse momentum vectors, $P_{||}$ is the longitudinal momentum component and P the momentum. At the SPS collider the ambiguity was resolved in most cases, because in 1/3 of the events one of these two solutions was unphysical ($x_W > 1$). In 1/3 more of events the two solutions could be distinguished by checking energy and momentum conservation in the whole event. From the above studies and from Montecarlo calculations, one found that at $\sqrt{s} = 630$ GeV the neutrino solution giving the smaller longitudinal momentum of the W was, in most cases, the correct one. Therefore one could reconstruct the W four-momentum with a high efficiency [12]. At the increased energy of the Tevatron Collider, this method doesn't work anymore, because the W's can have a large longitudinal boost . From Montecarlo studies we found that only in 63 % of the cases the right solution is the one which minimizes the longitudinal momentum of the W. If we restrict the leptons to be in the central detector region, this percentage becomes even smaller (53 %) and the two neutrino solutions have about the same probability. The chance to reconstruct the W momentum vector correctly is as large as the chance of being wrong.

1.4.4 Rapidity distribution of leptons from W decay.

One can bypass the problem by studying the pseudorapidity distribution of leptons coming from W decay, because the shift in the W rapidity will also influence the lepton rapidity, and see if the lepton rapidity distribution is sensitive to different structure functions [13]. In the W rest system the decay leptons have an angular distribution proportional to

$$(1 \pm \cos\theta)^2 .$$

There are two contributions defining the lepton rapidity distribution: one is the decay pattern of the W, given by the V - A coupling, the other one is the longitudinal momentum distribution of the W, due to its production mechanism. The V - A decay tends to emit positive leptons towards negative rapidities, while the production asymmetry tends to shift them to positive rapidity. If we assume that the V - A model is valid, the lepton rapidity distribution is directly related to the proton structure functions.

As a sensor of the lepton rapidity distribution, we choosed to study the lepton charge asymmetry projected on the positive rapidity axis, defined in the following way :

$$A(\eta) = \frac{N^+(\eta)-N^-(\eta)}{N^+(\eta)+N^-(\eta)}$$

where $N^+(\eta)$is the number of events with q(=lepton charge) x η(=lepton pseudorapidity) greater than 0 and correspondingly $N^-(\eta)$ the number of events with q x η less than 0. We find that this lepton charge asymmetry is sensitive to the structure of the proton at low x, and allows to test the existing structure functions in a flavor sensitive way. In fig. 1.8 we show the lepton charge asymmetry from W -- > l ν predicted in lowest order using several sets of structure functions. Comparing fig. 1.6 and 1.8, one can see that the larger asymmetries are predicted by the structure functions which have a steeper x-dependence of d(x)/u(x) in this x range ($0.02 < x < 0.12$).

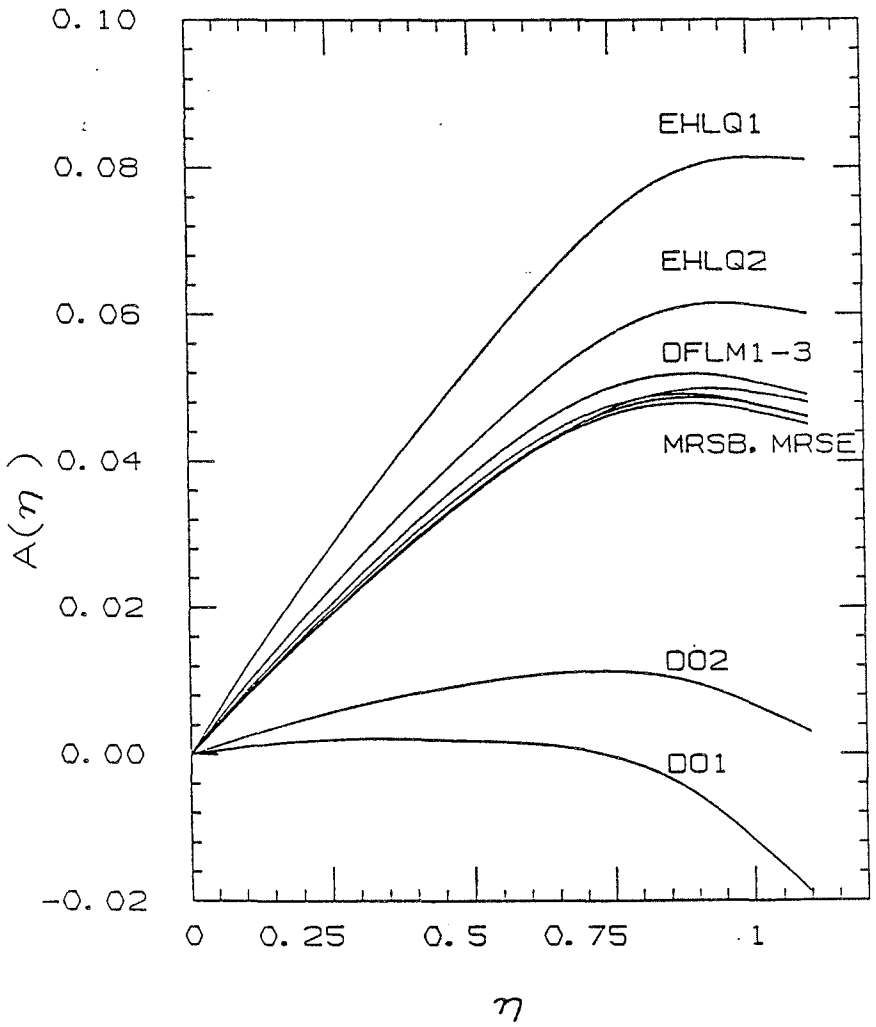

Fig. 1.8 Lepton charge asymmetry in W decay obtained from several structure functions.

The quantity that we measure is:

$$N_{\pm}(\eta_l) = \sigma_{\pm}(\eta_l) \cdot \varepsilon_{\pm}(\eta_l) \cdot \int Ldt$$

where $\varepsilon_{\pm}(\eta)$ is the detection efficiency. If we safely assume that the detection efficiency is charge independent (though it may be rapidity dependent), the detection efficiency at each η point cancels in A (η), so that the asymmetry function is detector independent. This allows us to directly compare theoretical predictions to experimental data.

Chapter II

The Experiment

2.1 The Tevatron

The Fermilab Tevatron Collider is currently the world highest energy accelerator, colliding protons with antiprotons at a center-of-mass energy of 1.8 TeV. It is a synchrotron employing superconducting magnets. The Tevatron shares the tunnel with the original Fermilab accelerator, called the Main Ring, using conventional magnets, which reached a maximum energy of 400 GeV. A schematic drowing of the Fermilab collider is shown in fig. 2.1.

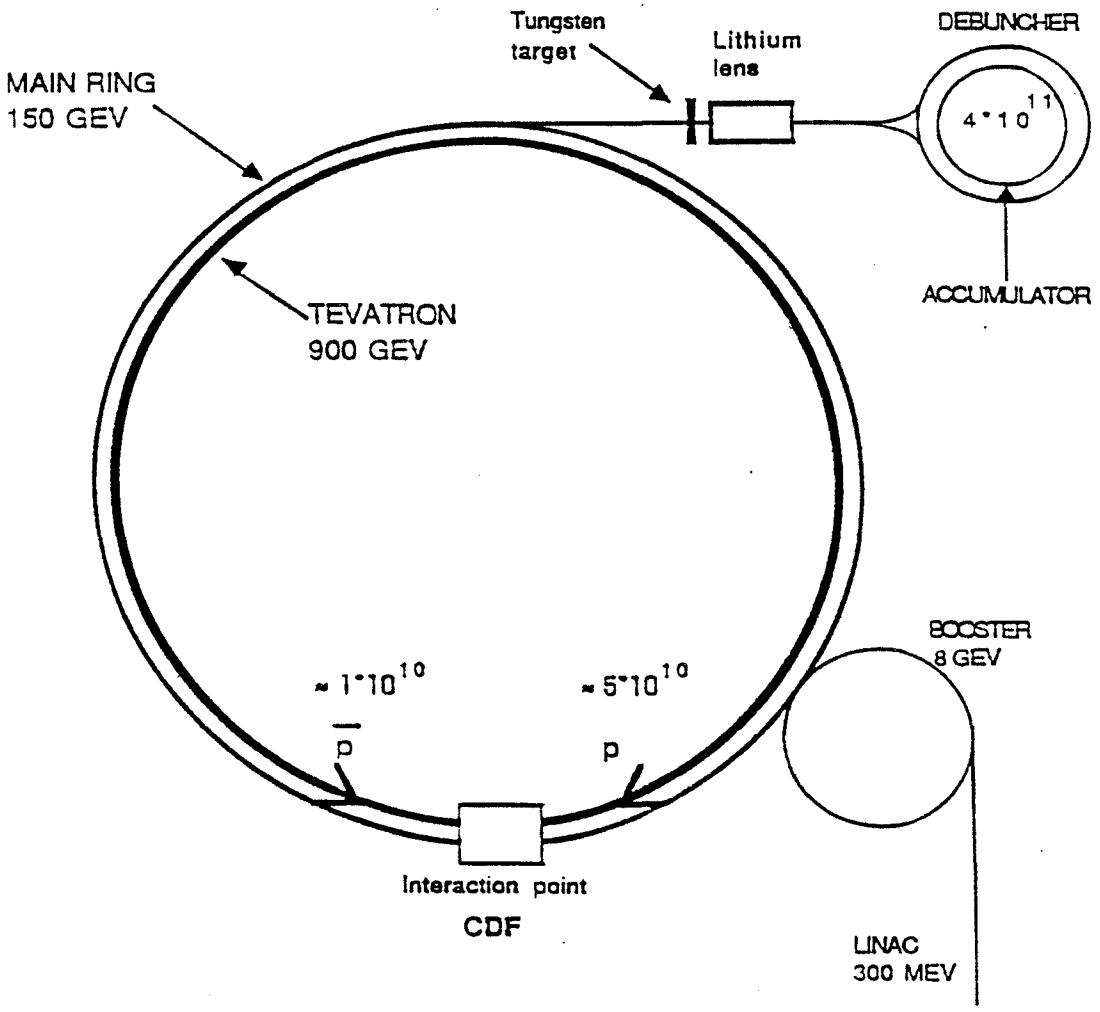

Fig. 2.1 Schematic view of the Fermilab synchrotron.

Protons are accelerated up to 900 GeV through several phases: first an electrostatic accelerator and a linear accelerator (LINAC) accelerate the protons to the energy of 200 MeV. Then protons are injected in a circular accelerator (BOOSTER) where they reach 8 GeV. From here, they enter the Main Ring, where they are accelerated up to 150 GeV. Finally they enter the Tevatron, where a strong enough magnetic field allows the beam to reach energies of 900 GeV. About 5×10^{10} protons per bunch are accelerated in this way in several bunches (six in the 1988-89 run).

The Main Ring provides also primary protons at 120 GeV to the antiproton source. They collide on a tungsten target and produce antiprotons. The antiprotons are created with a broad momentum spread. They are collected through a lithium lense after which they enter the Antiproton Debuncher-Accumulator complex. There the antiprotons are concentrated into dense bunches. After accumulation is completed, the bunches of antiprotons are injected into the Main Ring, where they are accelerated up to 150 GeV. Finally, they are sent to the Tevatron. There, they are accelerated together with the protons, in the opposite direction, to 900 GeV. The total number of antiprotons per bunch is about 10^{10}. All these steps are summarized in Table 2.1.

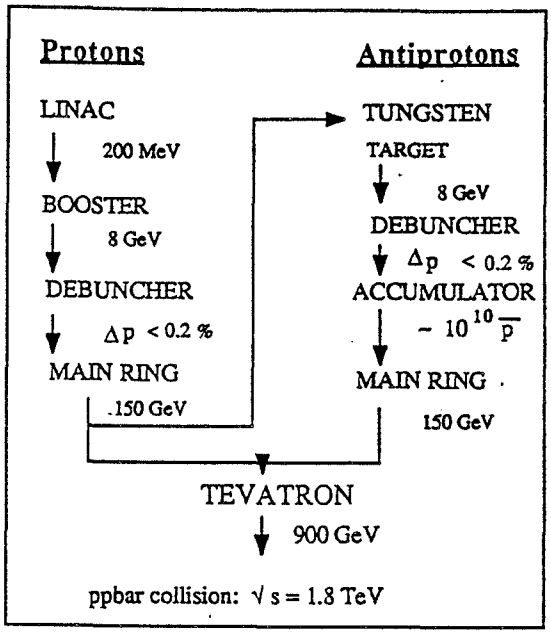

Table 2.1 $p\bar{p}$ path to the collision

The 6 bunches cross at 12 points around the ring. Eight focusing quadrupole magnets are inserted around the intersection points to reduce the beam size at the collision points.
Events occur at a rate:

$$R=\sigma L$$

where σ is the cross section for the process of interest and L is the collider luminosity. The properties of the stored beams determine L approximately as:

$$L = \frac{N_p N_{\bar{p}} C}{4\pi s^2}$$

where N_p and $N_{\bar{p}}$ are the numbers of protons and antiproton per bunch, C is the bunch crossing rate and s the transverse beam size. In the 1988-1989 run a luminosity of

10^{30} $cm^{-2}sec^{-1}$ was reached and surpassed. One presently aims at a luminosity of 6×10^{30} in the 1991 and 5×10^{31} in the 1995 run.

2.2 The Collider Detector at Fermilab

The Collider Detector at Fermilab (CDF) is a 4 π steradians general purpose detector. A perspective view and a side view of CDF are given in figs. 2.2 and 2.3. The basic goal of CDF is :

- detect charged particles and measure their momentum.
- measure the position and energy of electromagnetic as well as hadronic showers.
- identify leptons.
- observe indirectly non-interacting particles like neutrinos, by measuring the missing transverse energy.

In order to achieve this, the interaction region is surrounded by layers of different detector components. Particles encounter in a sequence tracking detectors, sampling calorimeters and muon detectors. The CDF polar coordinate system has the +Z axis along the beam line, in the direction of the proton beam. The azimuthal angle, ϕ, is defined with $\phi =$ 90o in the vertical upward direction. The polar angle, θ, is defined with $\theta =$ 0o along the +Z axis. The "natural" coordinate system for energetic hadrons are pseudorapidity, transverse momentum and azimuthal angle. For this reason an approximately cylindrically symmetric layout of the detector component has been choosen, with segmentation almost uniform in pseudorapidity (η) and azimuth (ϕ). CDF is built in three major pieces: forward and backward spectrometers, covering the region from 2° to 10° away in polar angle from the beams, and a central detector measuring particles at larger angles from the beam [15]. We will focus our attention on the central detector.

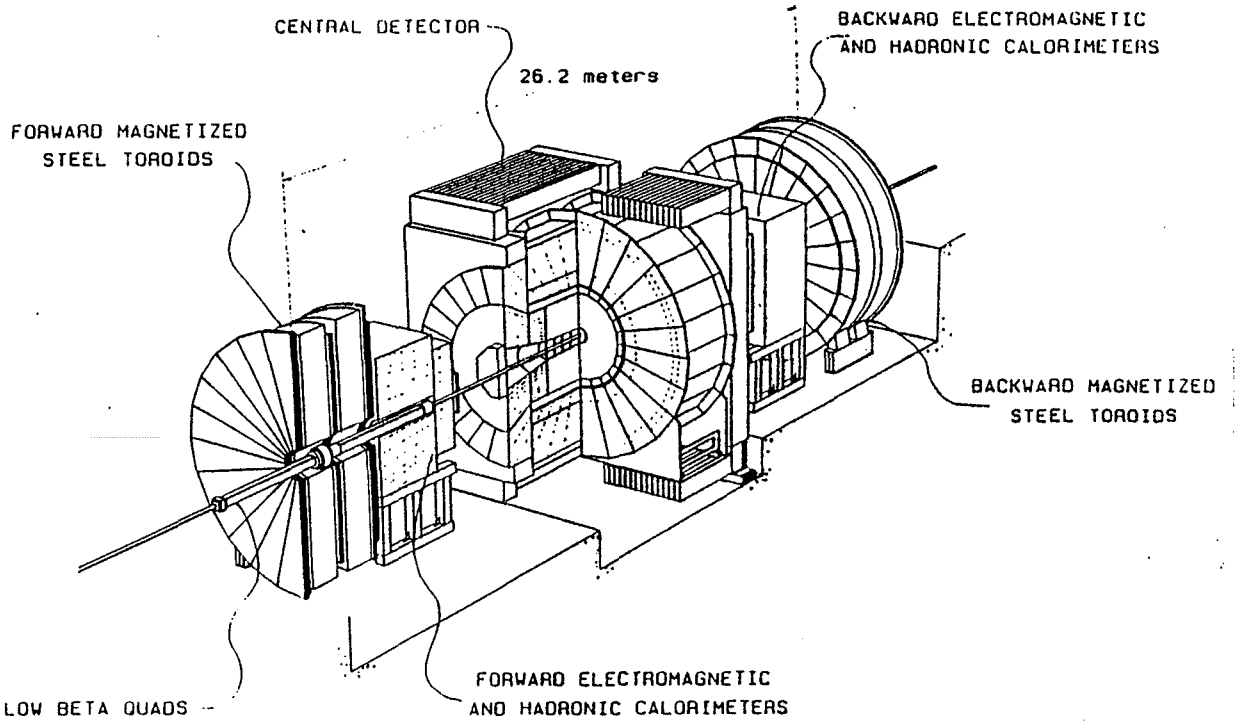

Fig. 2.2 A Perspective view of the CDF detector

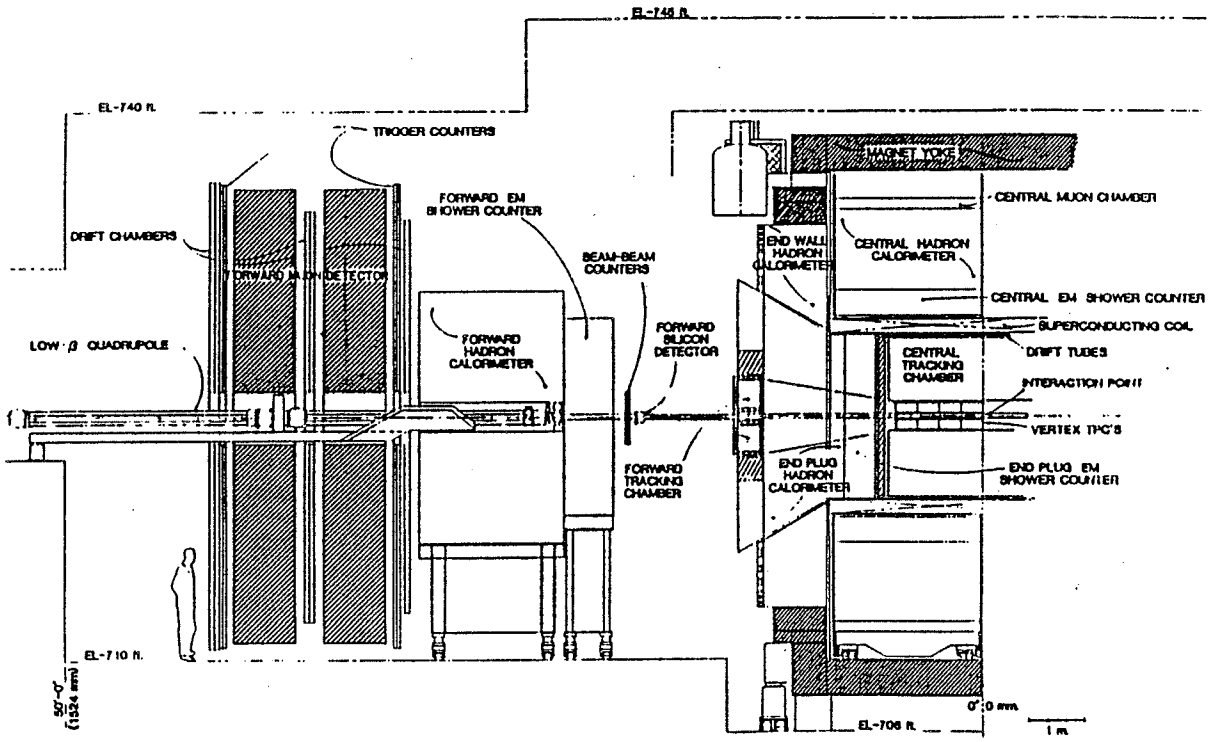

Fig. 2.3 Elevation view of the CDF detector.

2.2.1 The Tracking System.

The central tracking system is located inside the superconducting solenoidal coil. The solenoid provides a uniform magnetic field of about 1.4 Tesla, parallel to the beam axis. The magnetic field allows to measure charge and transverse momentum P_t of every particle, by measuring the bent trajectories with tracking chambers.

Surrounding the beam pipe, there is the Vertex Time Projection Chamber (VTPC), shown in fig.2.4 [16]. It consists of 8 adjacent octogonal chambers, which track charged particles at angles greater than approximately 3.5° from the beam line. They cover seven units in pseudorapidity ($-3.5 < \eta < 3.5$). The VTPC provides information on the event vertex and helps to identify events with multiple interactions in the same bunch crossing.

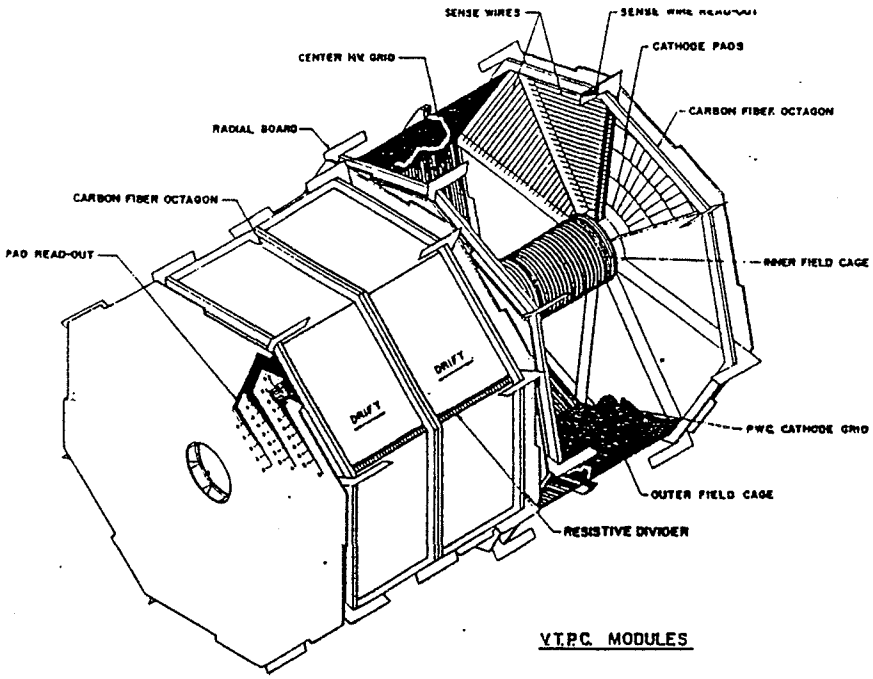

Fig. 2.4 Two of the eight Vertex Time Projection Chamber modules

On the outside of the VTPC there is the Central Tracking Chamber (CTC), a cylindrical drift chamber with inner radius 27 cm and outer radius 138 cm. [17]. The CTC gives precise momentum measurements in the central region $-1 < \eta < 1$. It consists of 9 super layers of sense wires. Five of these super layers have 12 wires parallel to the beam, providing tracking information in the r-ϕ plane (perpendicular to the beam). The remaining four stereo super layers contain 6 wires and are tilted by $\pm 3^{o}$ alternatively, with respect to the beam line. In addition to r-ϕ, they give track information in the r-z plane.

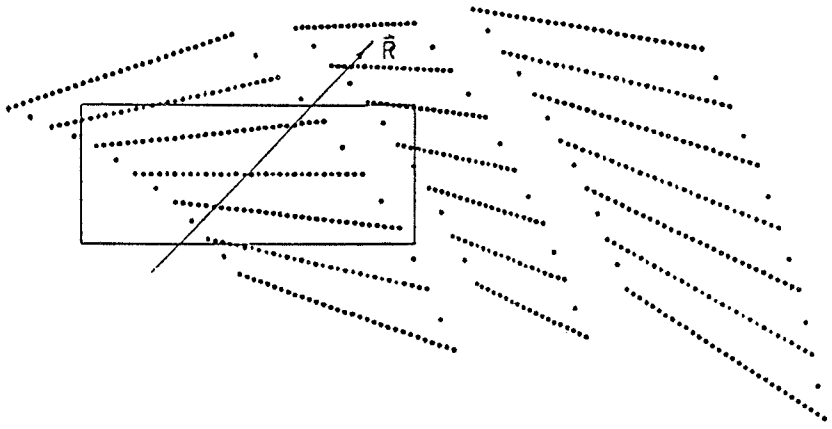

Fig. 2.5 Wire geometry for three cells in the innermost 3 superlayers.

As shown in figs. 2.5 and 2.6, the wires are arranged in cells, which are tilted to form an angle of 45o relative to the radial direction, to compensate for the Lorentz angle of the electrons drifting in the magnetic field. Tilting allows cells in the same superlayer to overlap in the radial direction, so that every radial (high Pt) track at some point passes close to one sense wire in each superlayer. This property is used to generate a prompt trigger signal for high Pt muon candidates. It also helps in the offline to resolve closely spaced tracks.

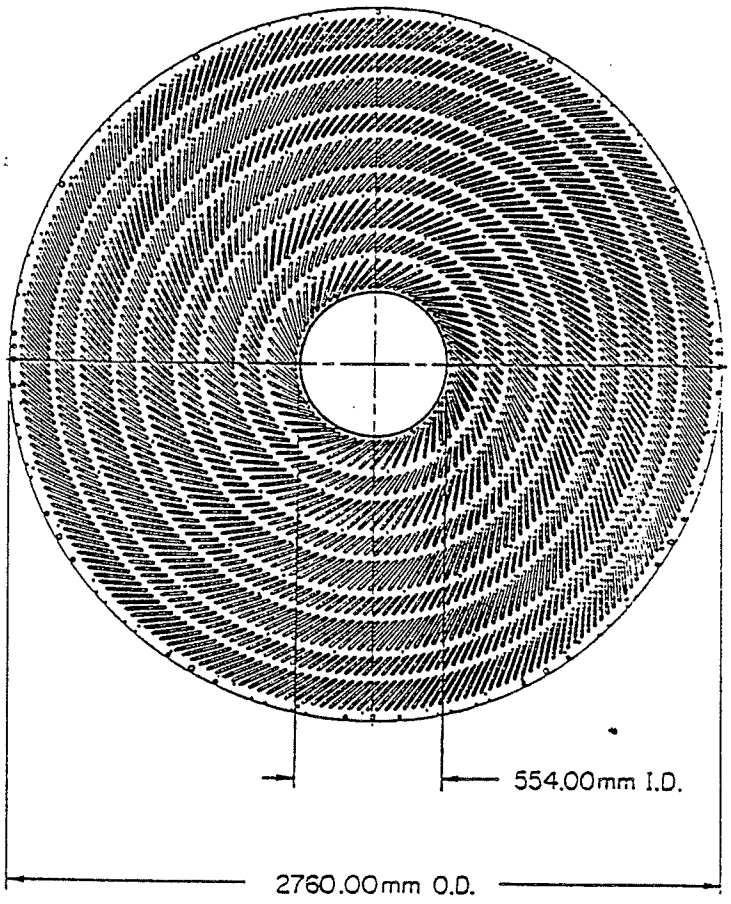

Fig. 2.6 The layout of wires in the Central Tracking Chamber showing the gouping into 9 superlayers and the 45° Lorentz angle.

The sense wires are read by multihit time-to-digital converters (TDC). A particle passing through the CTC causes a chain of hits along its path. The CTC reconstruction code provides tracks, which are reconstructed in the r-ϕ and in the r-z planes, fitting arcs of helicies to the hits detected in the chamber. If a charged particle has a transverse momentum smaller than 350 MeV, because of the magnetic field it spirals into the CTC and it does not reach the calorimeter.

On the outer perimeter of the CTC there are three layers of Central Drift Tubes (CDT), (fig. 2.7 [18]). For particles produced in the central region each tube at a location in phi provides high accuracy r-z tracking information, at a radius of 1.4 m from the beam line Both drift time and charge division are measured, potentially providing a more accurate Z measurement than the stereo layers of the CTC. Like the CTC, the CDT cover the region $-1 < \eta < 1$.

The performance specifications of the tracking system components are summarized in Table 2.2. Surrounding the CDT there is the superconducting coil, which is 0.85 radiation lengths thick.

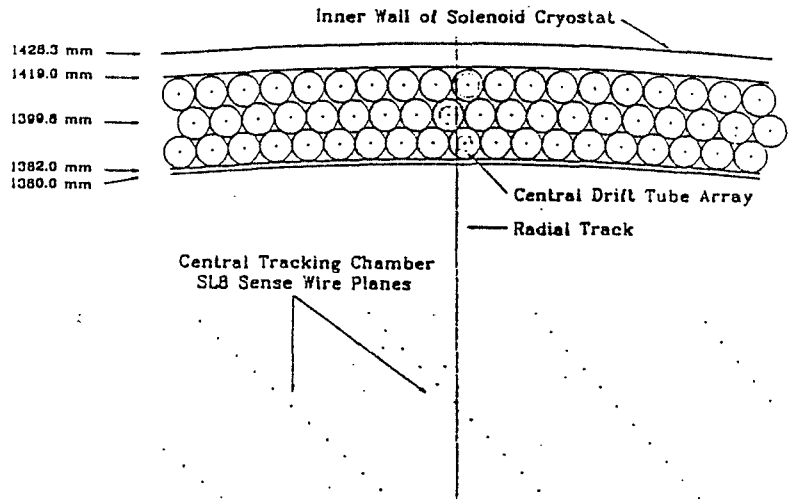

Fig. 2.7 A section of the Central Drift Tube (CDT) system showing the three layers of drift tubes . Also is shown the outer superlayer of wires of the CTC.

Tracking system	Number of sense wires	Spatial precision (per hit)	2-track resolution
VTPC	3072 wires	200-500 μm (0-15 cm drift)	6 mm / θ (Z) 6 mm (r) 3 cm (φ)
CTC	6156 wires	< 200 μm (r - φ) < 6 mm (Z)	3.5 mm
CDT	2016 wires	200 μm (r - φ) 2.5 mm (Z)	

Table 2.2 Tracking system performance specifications.

2.2.2 The Central Calorimeters

Outside of the magnetic coil there are the central electromagnetic (CEM) and central hadronic (CHA) calorimeters [19,20]. They are sampling calorimeters. Layers of sampling material are interleaved with layers of absorber. The CEM uses lead as an absorber, while the CHA uses iron. The shower energy deposits are summed over the sampling layers of the two separated EM and HAD sections. The calibration was determined in a test beam of particles of known energy and is checked using momentum analysed single particles in the experiment. CEM and CHA are divided into two polar halves at the plane Z = 0. Each

in the experiment. CEM and CHA are divided into two polar halves at the plane Z = 0. Each polar half is organized into 24 azimuthal modules, called 'wedges'. Each wedge contains a number of projective towers of size 0.1 in η and 15° in ϕ. This segmentation satisfies the demand for high granularity (the segmentation is fine enough that jets will normally spread over more than one tower) while minimizing cracks, that introduce dead regions between towers. The towers are projective: they point to the nominal collision point. A strip chamber embedded in CEM at a depth of six radiation lenghts greatly improves the position resolution for electrons and photons (CES). Wavelength shifters absorb blue light from the scintillator and transmit light of longer wave length to light guides. These run radially out of the calorimeter to photomultiplier tubes on the two azimuthal sides of each tower. The CEM extends from 168 cm to 208 cm in radial distance from the beam axis, providing a total of 20 radiation lenghts. It covers efficiently the region between $-1.1 < \eta < 1.1$. The single particle energy resolution is:

$$\frac{\sigma_E}{E} = \frac{0.14}{\sqrt{E_t}} + 0.017 \quad .$$

The resolution on the impact position of isolated electrons or photons is momentum-dependent, and varies from 3 mm at P_t=10 GeV/c to 2 mm at P_t = 50 GeV/c.

The central hadronic calorimeter surrounds the CEM. It covers the region in pseudorapidity $-1.3 < \eta < 1.3$. The CHA alternates 48 five cm thick layers of steel with scintillator planes and extends from 208 cm to 349 cm in radial distance from the beam axis, for a total of about 5 absorption lenghts. The single particle energy resolution of the CHA is

$$\frac{\sigma_E}{E} = \frac{0.80}{\sqrt{E_t}}$$

Signal collection for the CHA, although mechanically complex (see fig. 2.8), is logically identical to that of the CEM.

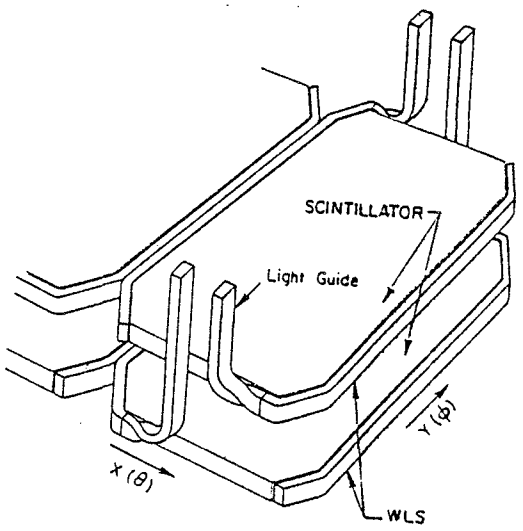

Fig. 2.8 Scheme of light collection in CHA calorimeter.

Jet reconstruction

High P_t partons emerging from the collision hadronize into jets. A jet is a collimated group of particles. The jet reconstruction algorithm looks for regions in $\eta - \phi$ space which show a concentration of energy deposit. The jet identification process occurs in two stages. First, a list of calorimeter towers with Et > 1.0 GeV is formed and pre-clusters are defined as chains of adjacent towers with continuously decreasing E_t. In the next stage, if the total energy of a pre-cluster is > 2 GeV, it is used as a starting point for clustering. The E_t weighted centroid of the precluster is calculated, a cone of fixed radius is formed around it and all the towers inside the cone whose E_t is greater than some threshold are included. This process is repeated until the list of towers which fall inside the cone remains unchanged. The jet 4-vector is formed using all the clustered towers: jet energy (momentum) is defined as the scalar (vector) sum of the tower energies.

Missing energy

Neutrinos do not interact with any detector component. Therefore they cannot be directly detected. This causes a transverse energy flow imbalance in the event. The missing energy is defined as:

$$\vec{E}_t = - \sum_i \vec{E}_t^i$$

where $\vec{E}_t^i$ is the vector energy deposition in a single tower of the CDF calorimeter and the sum is carried over all calorimeter towers. Minimun ionizing particles traversing the calorimeter, such as muons, deposit little energy in the calorimeter. For this reason they weight little in the $\vec{E}_t$ balance, very much like neutrinos. If there is a muon in the event, in order to get the true missing energy due only to neutrinos, the calorimeter $\vec{E}_t$ is corrected by:

$$\vec{E}_{t(mis)} = - \vec{P}_t^{\mu} + \vec{E}_t$$

where $\vec{P}_t^{\mu}$ is the transverse momentum of the muon.

A big fraction of the $p\bar{p}$ collision energy escapes undetected through the beam pipe. Longitudinal energy balance in the beam direction cannot be demanded. The longitudinal component of the neutrino momentum cannot be measured.

2.2.3 The Central Muon Chambers.

The central muon detector is located just outside the central hadron calorimeter, at a radial distance of 349 cm from the beam axis [21]. It uses wire proportional drift chambers to measure charged particle tracks exiting the central calorimeter wedges. Each central calorimeter wedge is backed by a set of three muon chambers bolted together at each end to form a single unit, for a total of 144 drift chambers. The muon chambers cover the central rapidity region $-0.7 < \eta < 0.7$. Fig. 2.9 illustrates the chambers in a wedge. A 2.4^o azimuthal gap between adjacent 15^o wide wedges is not covered. Each chamber consists of 4 layers in the radial direction. There are 4 drift cells per layer. Four sense wires, one from each layer, form a muon tower. One pair of these four wires, from alternating layers, lies on a radial line which passes through the interaction point. To avoid left-right ambiguity, the

remaining two wires of a tower lie on a line which is offset from the radial one by 2 mm at the midpoint of the chamber (see fig. 2.10).

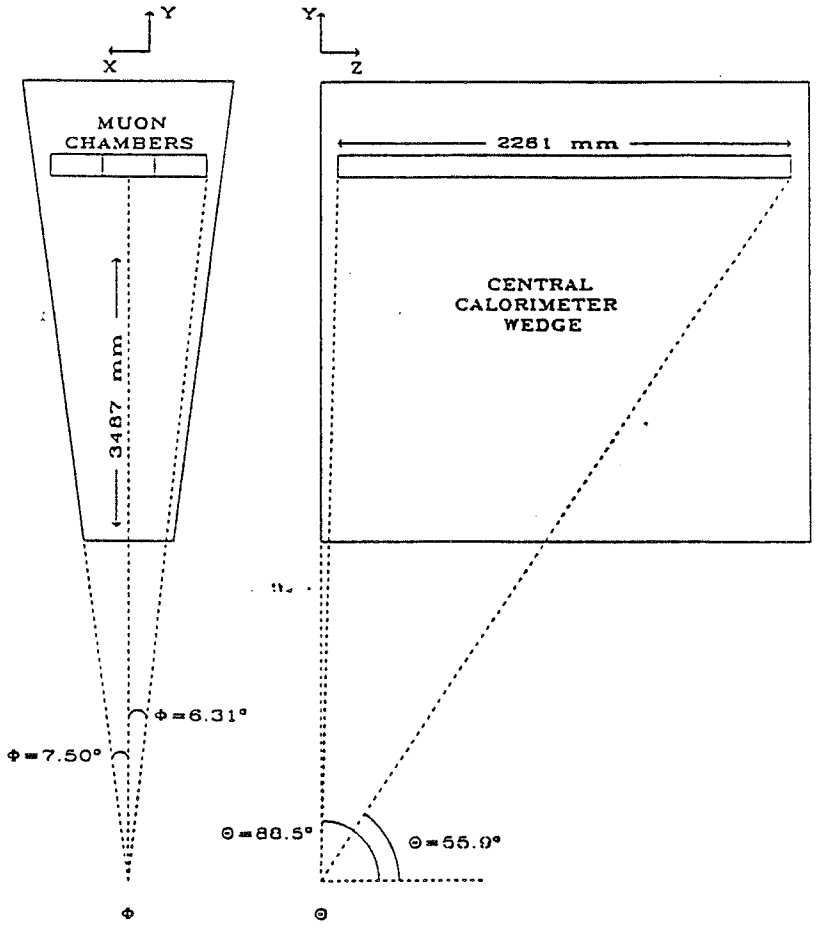

Fig. 2.9 The layout of the central muon chambers in one of the central wedges

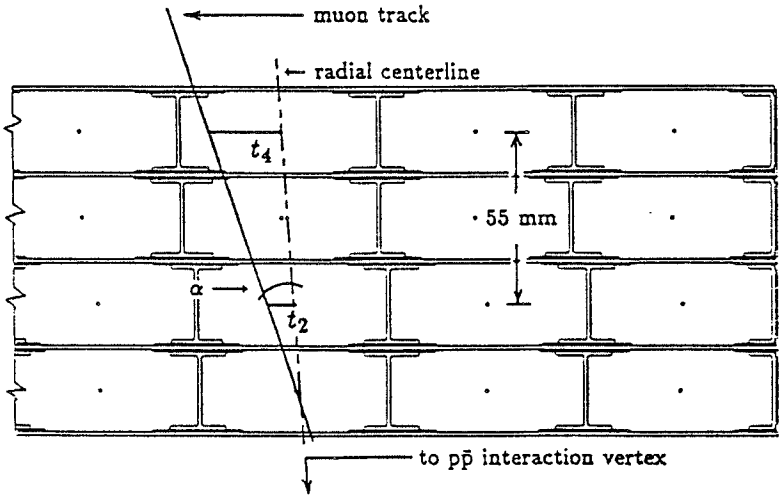

Fig. 2.10 The arrangement of the four planes of central muon chambers in a view along the beam direction.

The track angle with respect to the sense wire can be measured by comparing the arrival times of hits from alternating layers in the muon chambers. The track angle is related to the transverse momentum of the particle, since the solenoidal B field deflects tracks away from a radial line by an amount

$$\alpha = \frac{e\,L^2 B}{2\,DP_t}$$

where L is the radius of the solenoidal field, B is the field magnitude and D is the radial distance to the muon chambers (see fig. 2.11).

CMU tracks are reconstructed independently in the R - ϕ plane, using TDC information, and in the R -Z plane, by the use of charge division information. The position of a particle along the sense wire is found by the measurement of the charge deposited at each end of the sense wire.

When there are 4 hits in a tower, one assumes that a charged particle crossed the central detector and traversed the muon chambers. If at least three hits are present, a segment called 'stub' is reconstructed and if this stub corresponds to a track reconstructed by the CTC, then the track is labelled a 'muon '.

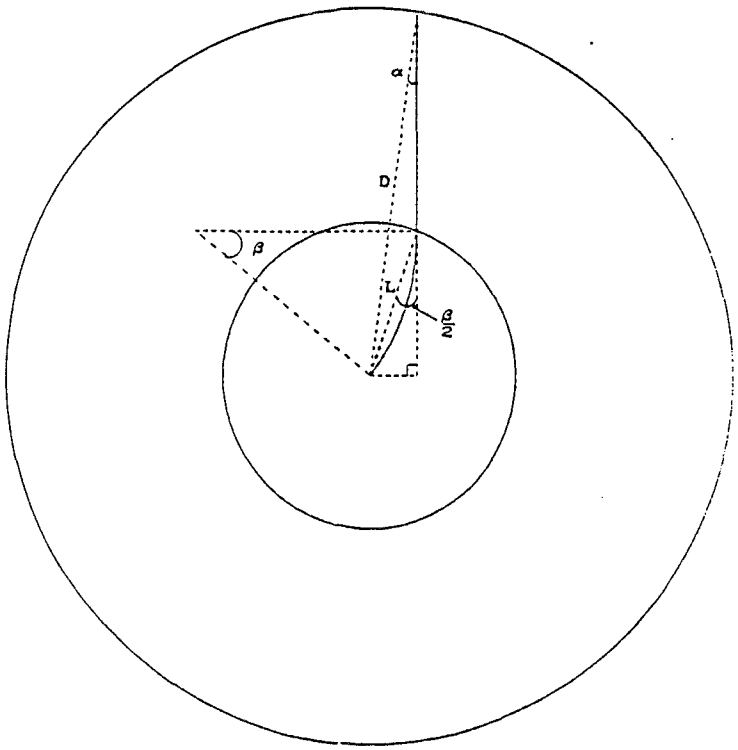

Fig. 2.11 Transverse projection of a charged particle track. The inner circle encloses the area where B= 1.4 T. The outer circle runs through the sense wires of the innermost muon chambers.

2.2.4 The Trigger.

The total cross section expected for $p\bar{p}$ collision at $\sqrt{s}$ = 1.8 TeV is about 80 mb. With a luminosity of $L = 10^{+30}$ ($cm^{-2}sec^{-1}$) = 1 $\mu b^{-1}sec^{-1}$, the rate of events is of the order of 80 KHz. . The rate at which data can be logged to tape is 1-2 Hertz, thus the trigger has to

reduce the events rate by a factor of 80000. In principle, this is acceptable since the rate of interesting events is a very small fraction of the total rate. For instance, the cross section for W production is 18 nb. However, the trigger must be capable, in a very short time, of rejecting the majority of the events while accepting interesting events with high efficiency. It also must be versatile enough to be changed during the run, depending upon the results of the experiment.

The CDF trigger is organized into four different levels, with a different timing at each level. The Beam-Beam counters (BBC) are two scintillator hodoscopes placed in front of the forward and backward calorimeters and provide a $p\bar{p}$ inelastic collision trigger (Level 0 Trigger). The inhibit following level caused data taking during the next beam crossing coming 3.5 μs later to be inhibited. Although this was a moderate problem during our past run, it will have to be changed for the future higher luminosity runs, when most bunch-bunch crossing will generate a candidate level 0 trigger.

The Level 1 Trigger decision was made within the 7 μs allowed by level 0. The Level 1 calorimeter trigger system computed the energy in the electromagnetic and hadronic calorimeters. For W electron candidates at least 6 GeV in a single trigger cell of the central electromagnetic calorimeter was required (a trigger cell combines two cells of the central calorimeter in the same wedge). The central muon level 1 trigger requires that hits from a central muon track be in coincidence with two of the four layers of the corresponding outer muon chamber. A cut on the time difference $|t_4 - t_2|$ or $|t_3 - t_1|$ between two radially aligned wires in a muon tower is imposed, where t_i is the drift time to the i-th wire in a muon tower (see Fig. 2.10):

$$\text{MIN}\,|(t_4 - t_2),(t_3 - t_1)| < t_{max},$$

and t_{max} is the time difference corresponding to the P_t threshold preset within the trigger table. A measurement of the trigger efficiency using cosmic rays showed that the efficiency for muon track finding in level 1 is above 90 % and independent of P_t for tracks with transverse momentum greater than 15 GeV/c (fig. 2.12). Level 1 delivered a rate of few KHz to the next level.

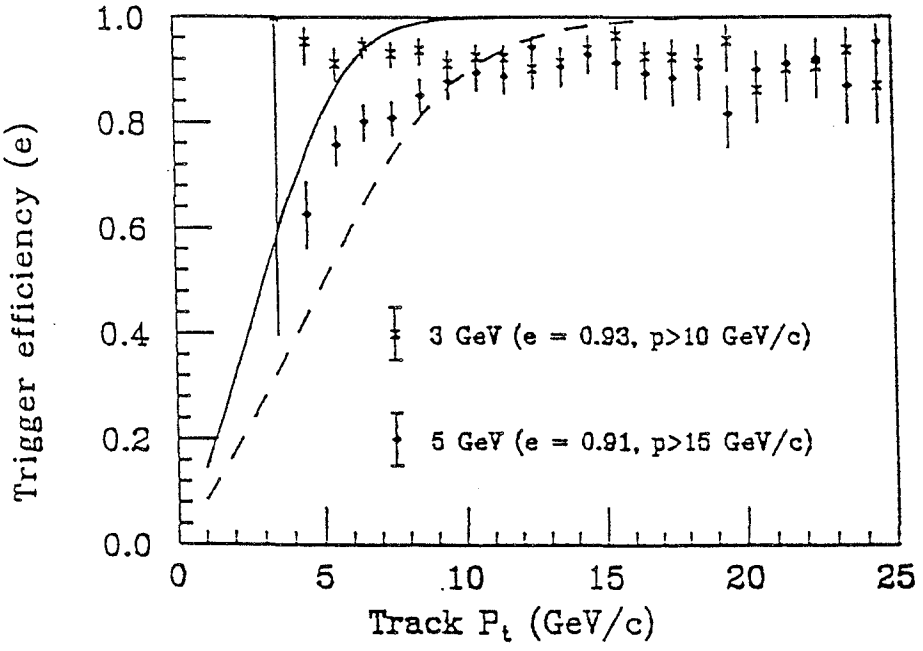

Fig. 2.12 The efficiency of the CMU Level 1 trigger as a function of track P_t for two different threshold. The solid and dashed lines show the predictions.

In level 2, both the electron and muon triggers use 2-dimensional tracks found by the Central Fast Tracker (CFT). This is a hardware track processor which uses fast timing information from the CTC to signal high transverse momentum tracks. The track finder analyzes prompt hits from the axial sense wires of the CTC to identify tracks by comparing the hits in the CTC to predetermined hit patterns for the range of transverse momenta allowed by the CFT trigger threshold. The list of found tracks is presented to the rest of the CDF trigger system for use in level 2 decisions.

The level 2 trigger selected central electrons if the following conditions were all satisfied:

1) a cluster transverse energy was found above 12 GeV,
2) a track found by the CFT, with nominal threshold $P_t > 6$ GeV/c, pointed towards the wedge containing the cluster,
3) less than 12.5 % of the energy in the cluster was in the hadron compartments.

The level two muon trigger requires that one track found by the CFT matchs a central muon stub. No calorimeter information was used to signal muon at this stage.

A level 3 trigger was also implemented during the 1988-1989 running period. This consisted of offline algorithms running on a farm of commercial computers. A fast, 2-dimensional track reconstruction algorithm determined the P_t and the ϕ of tracks at the radial distance of the muon chambers. Tracks above the P_t threshold of 9 GeV/c were matched to stubs identified by the muon level 1 trigger electronics within a 5° ϕ–window. If no match was found, the event was rejected. The level 3 electron filter required that the electron cluster, identified in level 2, be reconstructed with in software at least 12 GeV [3].

Chapter III

Montecarlo Predictions

3.1 The Papageno Montecarlo

To simulate W production at $\sqrt{s}$ = 1.8 TeV several Montecarlo programs are available. We used the Papageno Montecarlo.[22]. This is a partonic event generator which contains the correct matrix elements for W production and includes the W polarisation in the decay W --> l ν. It deals correctly with the Cabibbo suppressed reactions. It allows one to select the scale in the partonic process ($Q^2=\sqrt{\hat{s}}$), and to impose cuts on the outgoing primary particles. Papageno has ten different sets of structure functions available. We produced positive W's and we forced them to decay into leptons. Papageno produces electrons, not muons. We neglected the differency between W --> μ ν and W --> e ν. We assumed the W mass to be 80 GeV/c^2. In order to do some general studies, we used the three structure functions EHLQ1,MRS1 and DO1. For each of these structure functions we generated a high statistics sample (1.4 million events).

3.1.1 Expected Asymmetry for Pt(W) = 0

First we studied W's produced with Pt(W) = 0, and therefore with no associated jets. [23]. In order to show how the V - A decay pattern influences the lepton rapidity distribution, we selected a sample of W's produced almost at rest ($P_{\parallel} < 18$ GeV/c). In figure 3.1 we compare the rapidity distribution of leptons from this sample (broken histogram), to the rapidity distribution of leptons coming from W's with no cut on the longitudinal momentum (continous histogram).

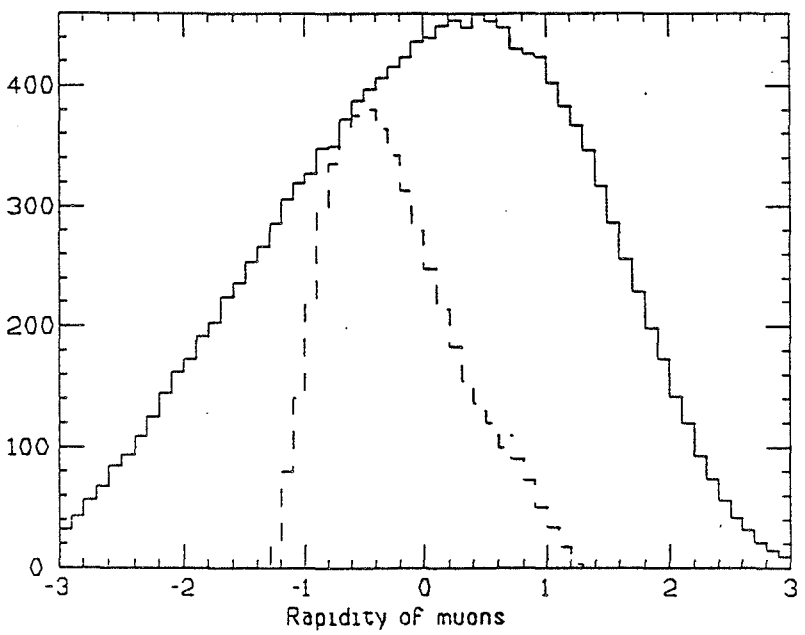

Fig. 3.1 Rapidity distribution of charged leptons from W decay.

We see that , due to the V - A asymmetry, W's at rest prefer to emit the lepton towars negative rapidities. However, the W production mechanism shifts the W's, and therefore also the decay leptons, much more towards positive values of rapidity. In the central region the production asymmetry overcompensate the decay asymmetry.

We plotted the previously defined lepton charge asymmetry versus lepton rapidity, for the three sets of structure functions. In order to get a cleaner W sample, we will have to apply a cut on the transverse lepton-neutrino mass, requiring $M_t > 50$ GeV/c^2 on the CDF data. Therefore we always apply this cut on the Montecarlo events as well. The pure V-A asymmetry should yield negative values for the asymmetry. This effect dominates at high rapidities, where the V - A asymmetry gets stronger. However, in the central region the production asymmetry dominates. The asymmetry distributions are different for different structure functions. Tightening the transverse mass cut will bias against leptons at large $|\cos\theta^*|$, where the V - A asymmetry is stronger. In figures 3.2, 3.3 we show the lepton asymmetry for two different cuts on transverse mass, respectively 40 and 50 GeV/c^2. EHLQ1 yields the largest asymmetry and DO1 the smallest one.

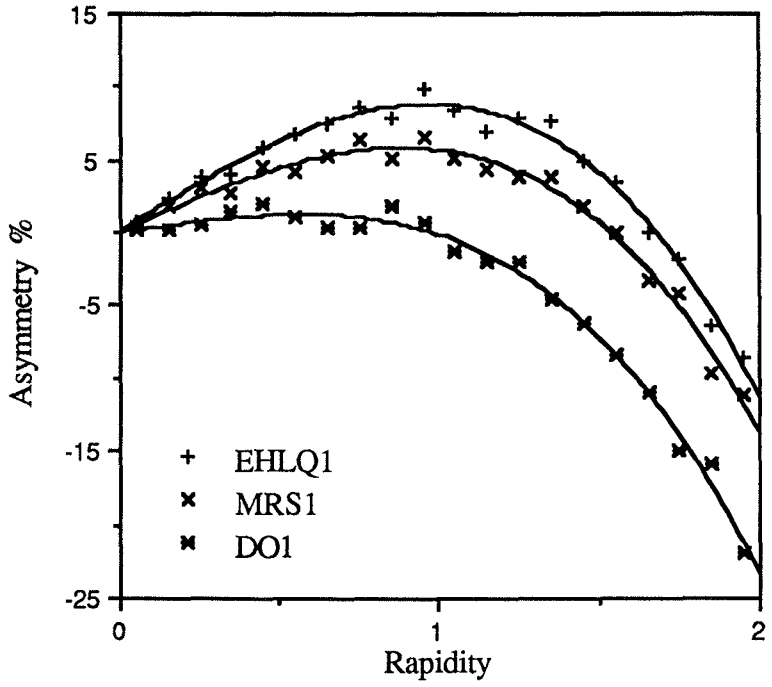

Fig. 3.2 Asymmetry versus lepton rapidity. Transverse mass greater than 40 GeV/c^2.

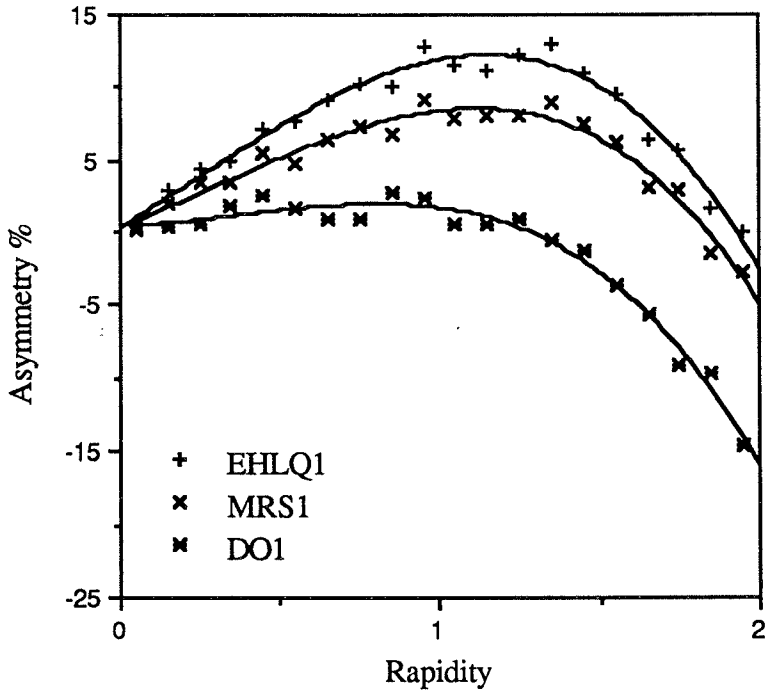

Fig. 3.3 Asymmetry versus lepton rapidity. Transverse mass greater than 50 GeV/c^2.

3.1.2 Independence of the Asymmetry of Pt(W)

In order to compare Montecarlo predictions to experimental data, we need to know how the asymmetry depends on Pt(W). We produced W + 1 Jet events with Pt (W) > 5 GeV/c for each of the three different structure functions. Papageno cannot correctly simulate W + 1 Jet events at Pt(W) between 0 and 5 GeV/c. Fig. 3.4 shows the asymmetry integrated over all values of rapidity, as a function of Pt (W). A cut was only applied on the transverse lepton-neutrino mass, requiring $M_t > 50$ GeV/c^2. In fig. 3.5 we required in addition | rap(lepton) | < 1.2. We fit a polynomial of third order to the data just in order to guide the eye. One sees that the asymmetry increases very weakly with Pt(W). Up to about Pt(W) = 20 GeV/c the asymmetry increases with a speed of about 0.5 % / 5 GeV/c.

Figure 3.6 shows the asymmetry as a function of lepton rapidity, for W's with transverse momentum between 5 and 10 GeV/c. The curves are very similar to those of fig. 3.2 . In figure 3.7 we compare the lepton asymmetry of W's with Pt = 0 and W's with Pt from 5 to 10 GeV/c (structure function EHLQ1). Within the available statistics, there is no significant difference between the shape of the two distributions. From the experimental point of view, it is easier to use low Pt W 's because the background is smaller and W's are easier to identify and to study [24].For our analysis we will use low Pt W's. The uncertainty brought in by the fact that Pt(W) $\neq$ 0 is not important for this sample. We will compare the observed asymmetry to lowest order predictions and eventually apply a small correction to take the effect of Pt(W) > 0 into account.

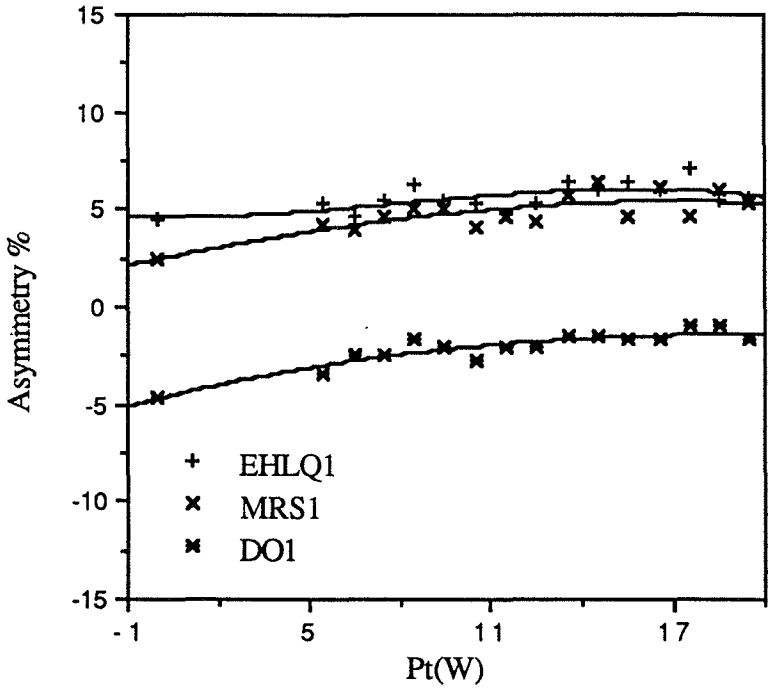

Fig. 3.4 Asymmetry versus Pt(W) (in GeV/c) integrated over all rapidities

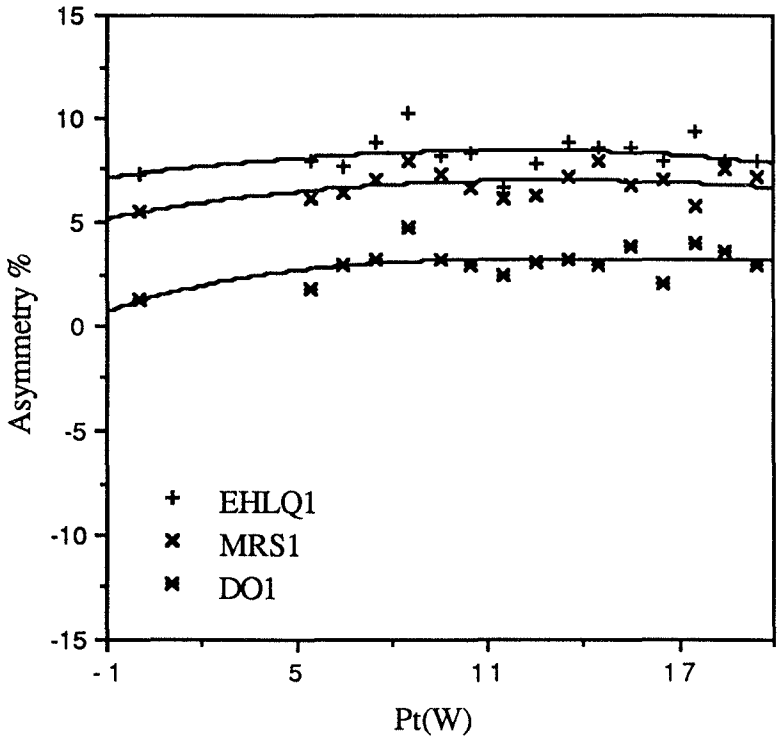

Fig. 3.5 Asymmetry versus Pt(W). Central rapidities. (abs(η) < 1.2).

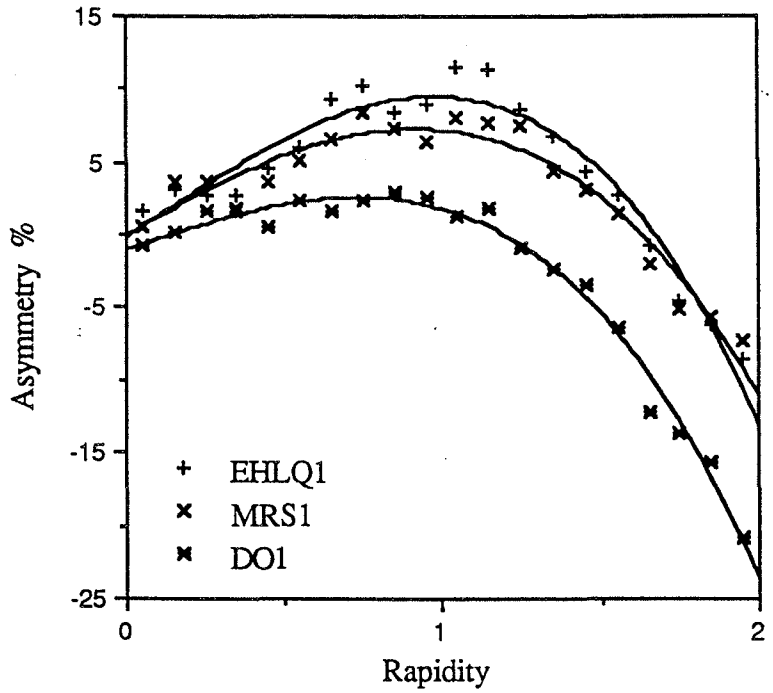

Fig. 3.6 Asymmetry versus lepton rapidity. Transverse mass greater than 40 GeV/c^2 and Pt(W) between 5 and 10 GeV/c.

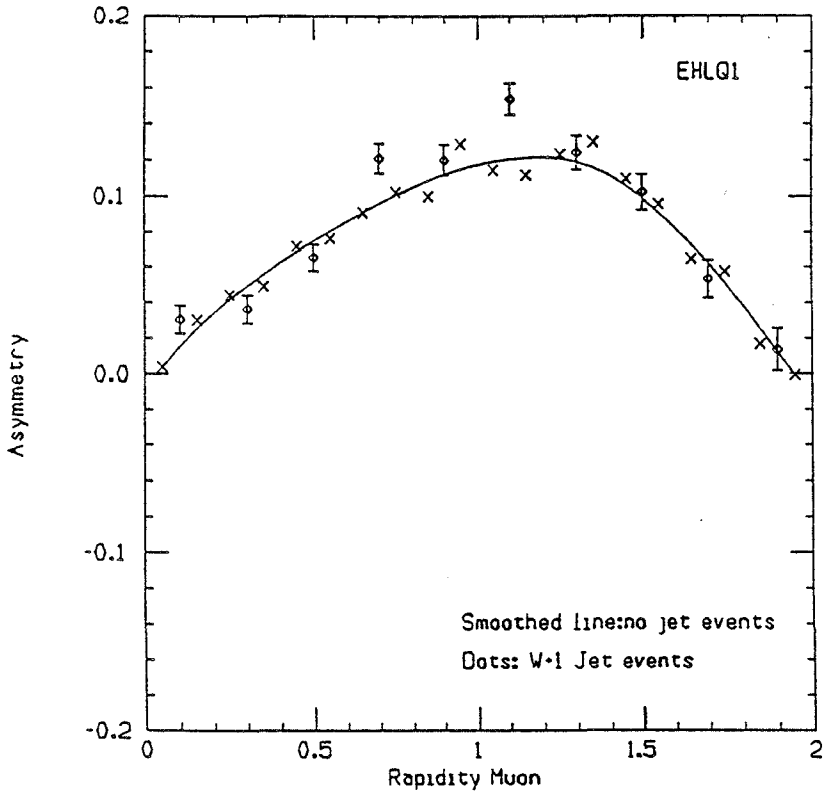

Fig. 3.7 Asymmetry versus lepton rapidity. Mt > 50 GeV/c^2.

3.1.3 Expected Jet rapidity distribution.

Because the W's are produced asymmetrically, one might suspect the associated jet to show a rapidity asymmetry as well. The jet asymmetry is defined in close analogy to the lepton asymmetry:

$$A = \frac{N^+ - N^-}{N^+ + N^-}$$

where N^+ (N^-) is the number of jet at charge(lepton) x rapidity(jet) > 0 (< 0). We applied the following cuts:

- jet rapidity < 4
- lepton rapidity < 0.7
- transverse momentum of jet > 7 GeV/c
- transverse lepton-neutrino mass > 40 GeV/c^2

Figure 3.8 shows the jet asymmetry as a function of Pt(W), for three different structure functions. One can see a slight dependence on Pt(W). Figure 3.9 shows the asymmetry as a function of jet rapidity. The curves are fits to guide the eye. The differences associated with different structure functions are modest. It's not clear whether the data would be able to distinguish among them. Furthermore, at higher values of rapidity it might be difficult to detect jets, and at high values of Pt(W) backgrounds become difficult to handle. For all these reasons we decided not to use the jet asymmetry to test structure functions.

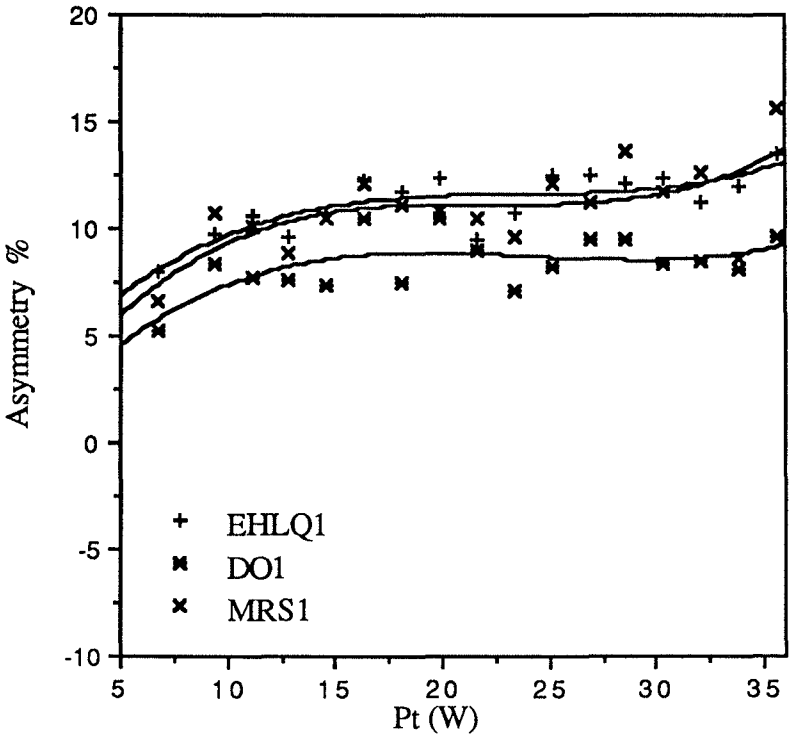

Fig. 3.8 Jet asymmetry versus Pt(W) (in GeV/c).

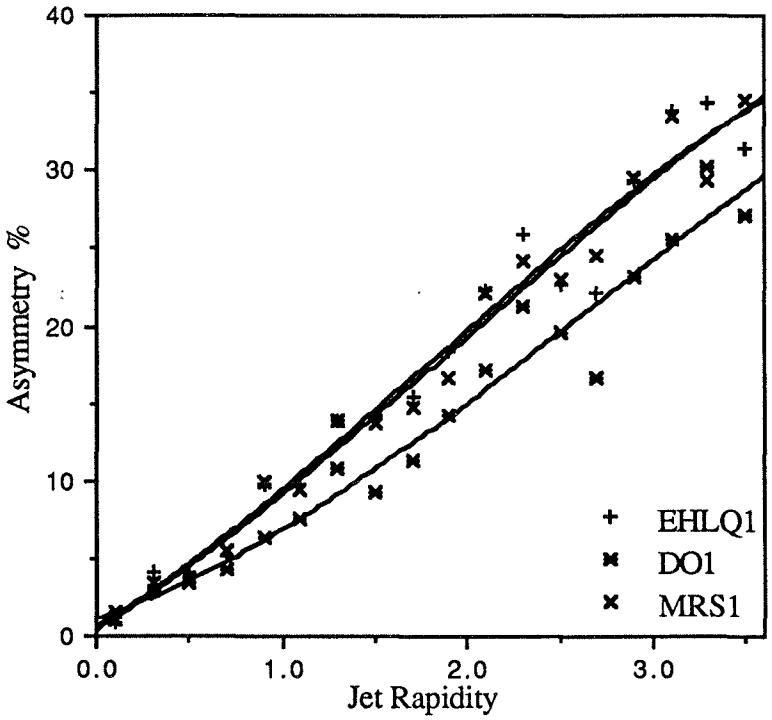

Fig. 3.9 Jet asymmetry versus jet rapidity.

Chapter IV

Data analysis

4.1 Data sample and data processing.

During its first high-luminosity run in 1988-89 the accelerator delivered an integrated luminosity of 9 pb^{-1}. About 5500 nine-track tapes of raw data, corresponding to 4.4 pb^{-1}, have been recorded by CDF. Each tape contains on average 1150 events. The raw data go through a "production" analysis at Fermilab which generates physics oriented output streams (such as electrons, missing energy, QCD etc.). This data is written on data summary tapes (DSTs). The inclusive muon sample consists of 1430 tapes. The muon data have been copied on 8 mm cassettes (almost 10 tapes per cassette) and distributed to various institutions, among them INFN Pisa. The size of the data set is large. There is the need of a smaller, more manageable data set, without loosing information which is relevant for our work. The following analysis is based on 'EVCON format' events, processed at INFN Pisa. 'Evcon' is a software package which condenses data to about 5 blocks per event. Each event is reduced to an array of unformatted numbers which contains what is beleived to be all the useful physics informations from the data banks. At the beginning, all the event with a reconstructed muon candidate are kept, without any additional cut. In a next step some cuts are applied on the inclusive muon sample, to further reduce its size.

4.2 Inclusive muon sample.

4.2.1 Muon identification

Muons are minimun ionizing particles. They do not shower in the electromagnetic calorimeter, and they do not interact strongly in the hadronic calorimeter. Fig. 4. 1 is a plot of the CEM energy deposition for 57 GeV/c muons from a test-beam. The energy deposition has a mean of 0.3 GeV. Fig. 4.2 shows the CHA energy deposition. The mean energy deposition in the CHA is about 2.1 GeV. One can see that $E_{CEM} > 0.5$ GeV and $E_{CHA} > 3.5$ GeV are unlikely [25]. Requiring the muons to be isolated and consistent with a minimum ionizing particle, we reduce the technical background coming from jets. The signature of an isolated high Pt muons in the CDF detector is a high-pt track in the CTC, minimum ionizing energy deposition in the calorimeters and a short muon track ("stub") in the central muon chambers, which matches the extrapolated central track to within multiple scattering errors (see section 4.3.3).

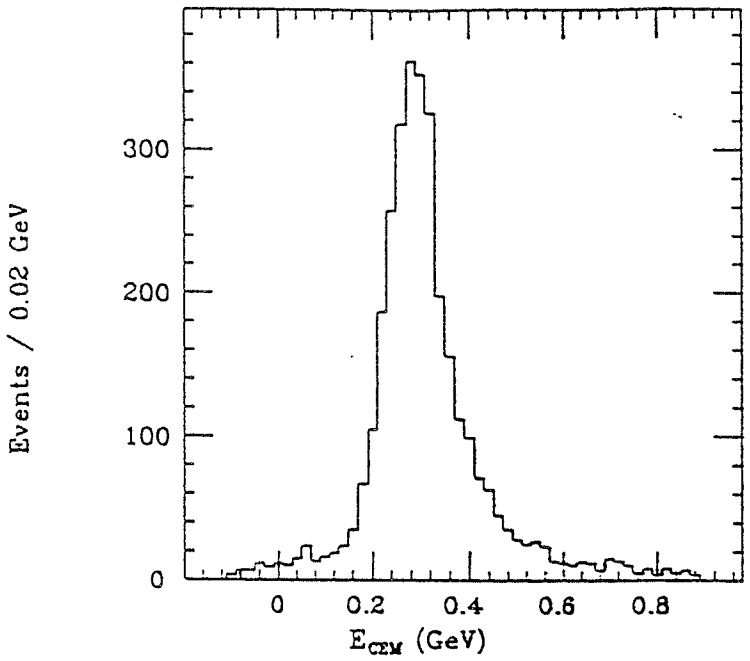

Fig. 4.1 CEM energy deposition for 57 GeV/c Test Beam Muons.

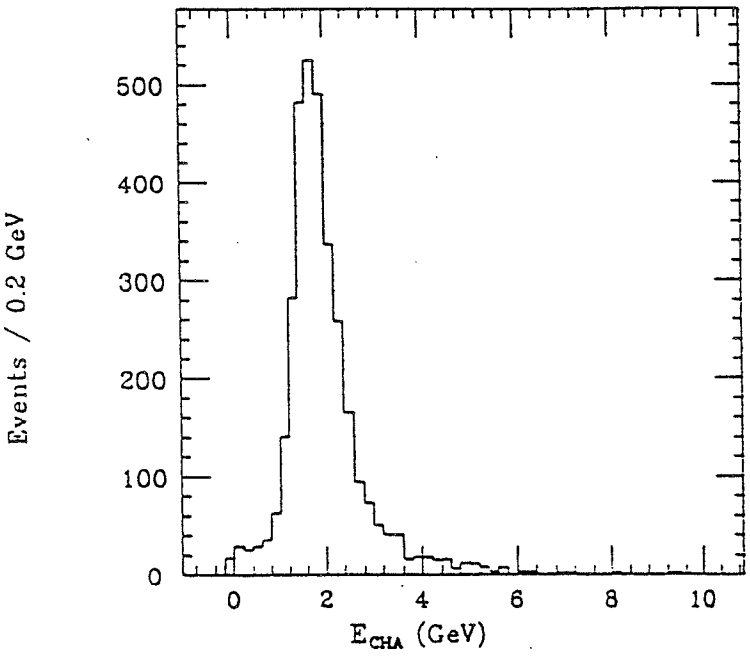

Fig. 4.2 CHA energy deposition for 57 GeV/c Test Beam Muons.

4.2.2 Technical Backgrounds.

We shall call technical background the background which arises because of some wrong interpretation of the measured parameters. In contrast, physical background may arise from a wrong assignment to some physics process of a correctly reconstructed event.

The inclusive muon sample has various contributions from several kinds of technical backgrounds, such as decays, punchthrough, leakage or misassociation.

Decays

Kaons and pions can decay into muons inside the CTC or in the calorimeter. Muons coming from hadron decays have lower momentum than the parent hadrons. These muons will suffer more multiple scattering in the calorimeters and their extrapolation through the magnetic field will scatter more relative to the observed stub. They might also be reconstructed with a wrong Pt, due to a kink in the CTC track.

Punchthrough

Hadrons might punchthrough the calorimeter without undergoing hadronic interactions. Such particles cannot be distinguished from real muons. The probability for a hadron to traverse one hadronic interaction lenght of material without strongly interacting, is 1/e. The CDF calorimeter consists of almost 5 hadronic interaction lenghts. Therefore the probability that an hadron does a non-interactive punchtrough and arrives at the muon chambers is about $e^{-5} = 0.0067$

Leakage

There is the possibility that particles in a jet shower in the last layers of the calorimeter. If the hadronic cascade is not completely contained inside the calorimeter, high energy jets can leak into the muon chambers and leave a track there.

Misassociation.

If there are several tracks in the central detector, it could happen that the software reconstruction chooses the wrong one and associates it with a muon stub (central track-central muon mismatch).

Fig. 4.3 shows the Pt spectrum of part of our inclusive muon sample. The Pt spectrum is steeply falling. Muons from W decay should exibit a jacobian peak. In order to select W-events, we have to eliminate the above sources of background. In most cases high Pt hadrons are part of a jet. We therefore reduce hadron punchthrough by requiring isolated muons which have a good matching between the CTC track extrapolation and the muon chamber stub. Also requiring a large missing transverse energy in the event reduces this background.

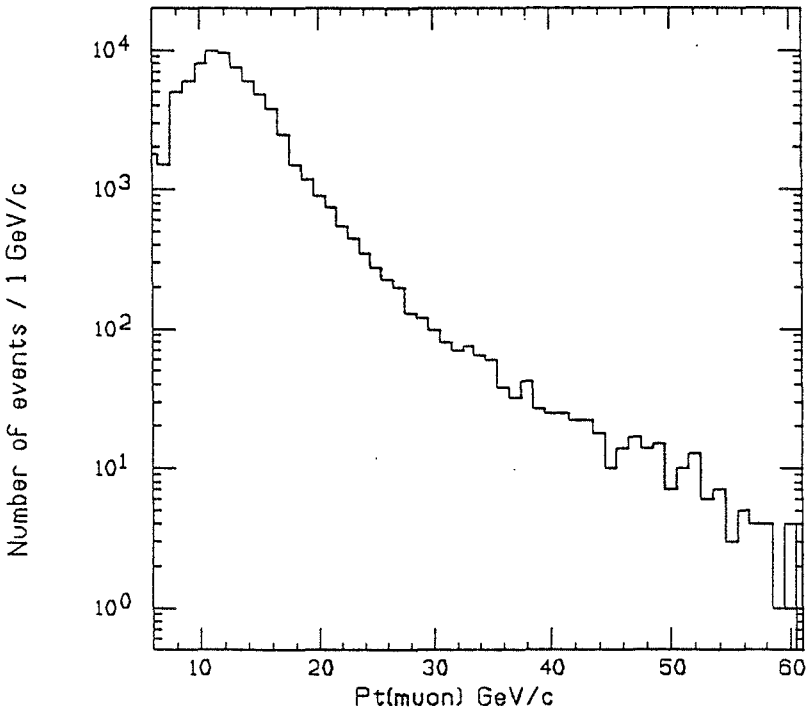

Fig. 4.3 Pt spectrum of part of the inclusive muon sample.

4.3 W event selection.

Our purpose is to identify and select W's. In order to achieve this goal, we apply cuts on both technical variables and kinematical event properties. We require events with high quality isolated muons and missing energy. The following sections describe the details of the cuts applied to the data. In order to investigate the effect of these cuts either Montecarlo studies or the data sample itself will be used, by loosening each cut individually while applying all the others. We keep only events which fired the central muon trigger. We reject events with interaction vertices more than 60 cm away from z =0. In order to improve the momentum measurement resolution a beam constraint was imposed, including the interaction vertex in the fit of the track.

4.3.1 Transverse muon momentum distribution.

In fig. 4.4 we show the Pt spectrum predicted from Montecarlo for charged leptons coming from W decay. Most of them (87 %) have Pt greater than 20 GeV/c. Decay kinematics imply that the Pt of the muon from W decay should be peaked toward $M_w/2$. Therefore, as first we apply a cut on transverse muon momentum, requiring P_t (muon) > 20 GeV/c.

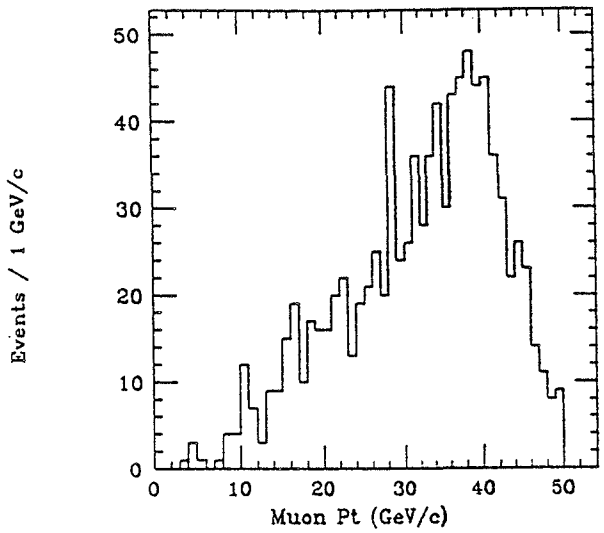

Fig. 4.4 Montecarlo Pt distribution of muons from W decay

4.3.2 Isolation variables.

In order to define the muon isolation, we consider a cone with radius expressed in terms of the azimuthal angle θ and of the pseudo-rapidity η as follows:

$$R = \sqrt{(\Delta\phi)^2 + (\Delta\eta)^2}$$

We select events whose muon candidate deposited less than 2 GeV of energy in the electromagnetic calorimeter and less than 5 GeV in the hadronic calorimeter, in the tower traversed by the muon, with R < 0.13. In fig. 4.5 we show the total transverse energy in a cone of radius 0.7 around the muon for the W sample. For real W events, there should be very little transverse energy in such cone surrounding the muon, as contributed by the soft underlying event.

We required the sum of electromagnetic and hadronic transverse energy in the cone of radius 0.7 including the muon to be less than 5 GeV. We also required the total energy in the muon tower to be greater than 0.5 GeV, in order to reject cosmic events which arrive out of time with the beam crossing.

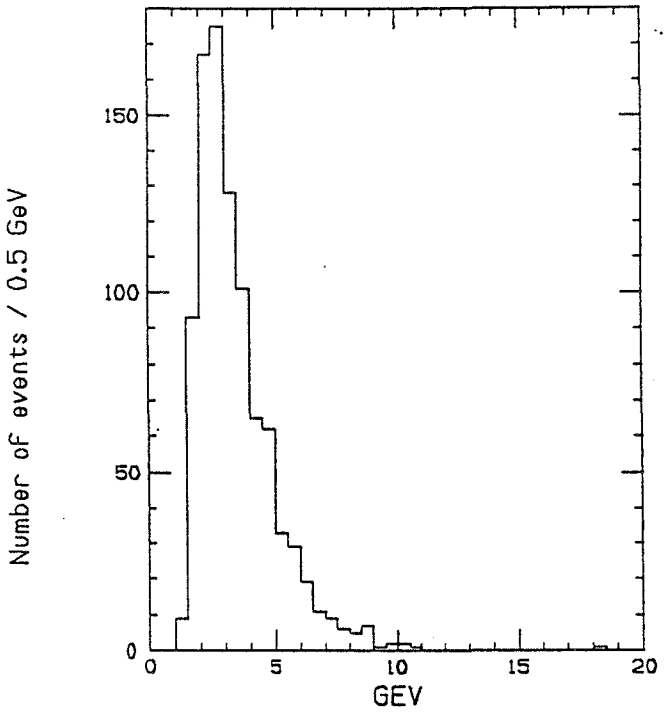

Fig. 4.5 Total transverse energy in a cone of radius 0.7 around the muon.

4.3.3 Matching variables

In order to link CTC tracks with muon stubs, we extrapolate the track outside the CTC through the calorimeters and into the chambers. Real muons do not follow the ideal path between the CTC and the CMU sketched in figure 2.11. They undergo multiple scattering. The muon will emerge from the calorimeter at a different position and with a different slope with respect to the extrapolation of the CTC track. The following variables are used to define the CTC-CMU track match:

- Δx distance in the r - ϕ plane (= x - y plane) between the CTC track extrapolation and the muon stub.
- Δz same distance, measured in the r - z plane
- Δxslope difference between the slope of the CTC track extrapolation and the measured slope of the muon stub in the transverse plane.
- Δzslope same slope difference, measured in the r - z plane.

For multiple scattering the angular and spatial deviations from the correct trajectory can be expressed, neglecting Moliere's tails [27], as a Gaussian distribution, centered at the value of the ideal path. The expected multiple scattering error on the matching distribution is respectively:

$$\sigma_{\Delta x} = \sigma_{\Delta z} = \frac{15}{P_t}\ \text{cm} \qquad (P_t \text{ in GeV/c})$$

$$\sigma_{\Delta xslop} = \sigma_{\Delta zslop} = \frac{0.12}{P_t}\ \text{radians} \qquad (P_t \text{ in GeV/c})$$

where P_t is the transverse momentum of the particle. The numerical factors were found using $P = P_t \sin\theta$ and averaging over the θ coverage of the muon chambers. For muons with $P_t > 20$ GeV/c, the multiple scattering gives an error:

$$\sigma_{\Delta x,\Delta z} < 0.75\ \text{cm}$$

$$\sigma_{\Delta xslop,\Delta zslop} < 0.06\ \text{rad}\ .$$

In addition to multiple scattering, bad matching can be due to hardware or software problems. For example an error on the P_t measurement can generate a CTC - CMU mismatch. Another source of error can come from a possible CMU chamber misalignment with respect to the CTC. In fig. 4.6 we show the Δx, $\Delta xslop$ and Δz distributions for good muon events.
The muon W candidates are required to have:

$\Delta xy < 2.5$ cm and

$\Delta z < 5.0$ cm .

The Δz cut is looser than the Δx cut, because the z resolution of both the CTC and the muon chambers is worse than the x-resolution.

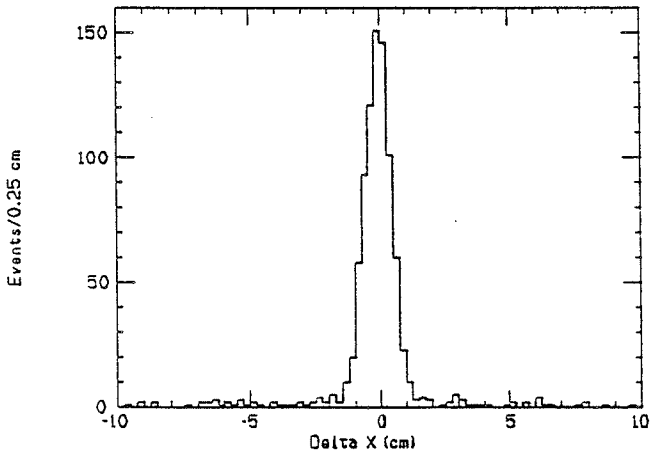

Fig. 4.6 a) Δx matching distribution, in cm.

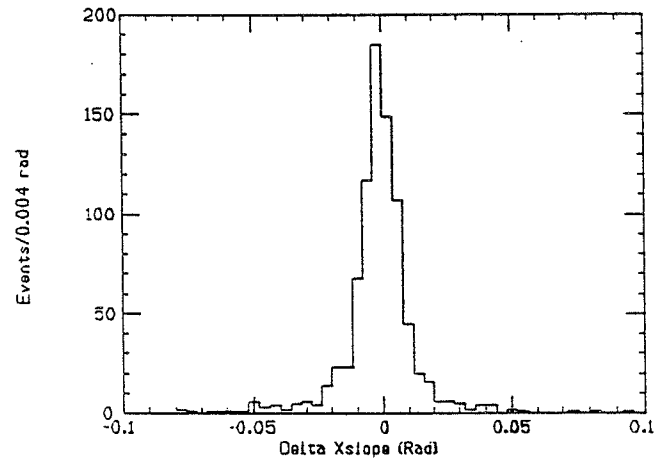

Fig. 4.6 b) Δxslope matching distribution, in rad.

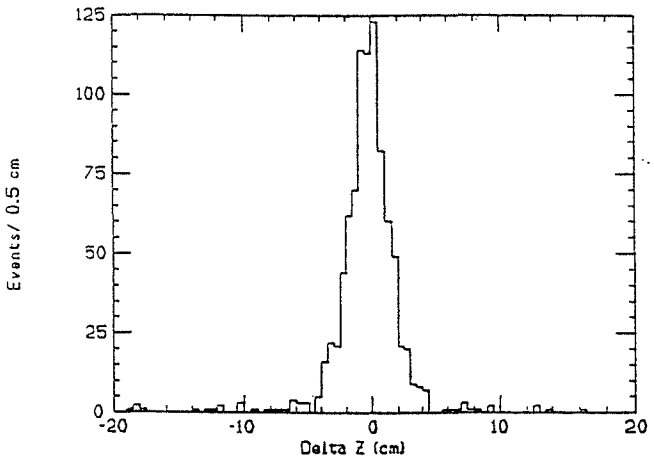

Fig. 4.6 c) Δz matching distribution, in cm.

4.3.4 Rejection of cosmic rays.

Cosmic rays can coincide with a beam bunch crossing. At large P_t they are a significant background to the muon sample. If a cosmic ray passes close to the intersection point it could mimic a high Pt di-muon event. If one branch is lost due to reconstruction problems, a cosmic ray might also mimic a W decay. In figure 4.7 we show the cosmic ray Pt spectrum [26]. In order to eliminate cosmic rays, we rejected events with a track back-to-back to the muon and Pt > 10 GeV/c. We also reject events with two muon stubs which are back-to-back in ϕ and in Z.

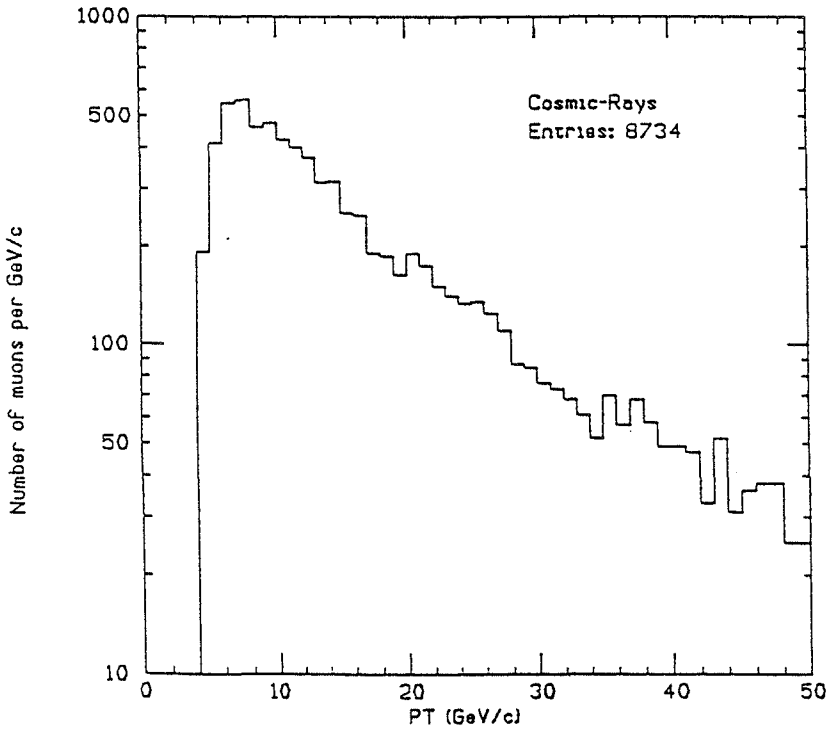

Fig. 4.7 Pt spectrum of the cosmic ray sample.

4.3.5 W transverse mass distribution.

Because the longitudinal component of the neutrino momentum is not known, we cannot measure the invariant mass of the muon-neutrino pair. We define the transverse mass of the W as:

$$M_t = \sqrt{2\,(E_t^{\mu} E_t^{\nu} - \vec{P}_t^{\mu} \cdot \vec{P}_t^{\nu})}$$

where E_t is the transverse energy and P_t is the transverse momentum vector. In fig. 4.8 we show the predicted transverse lepton-neutrino mass for leptons coming from W decay. The observed M_t distribution depends on the W transverse momentum distribution, on the detector smearing (resolution) of the lepton momenta and on the geometrical acceptance of the detector. We require the transverse mass to be greater than 50 GeV/c^2. This cut makes the data sample reasoneably free from jet background. It also helps to reject muons coming from τ decay. Because the momentum resolution gets worse for very high Pt muons we apply an upper cut on the transverse mass distribution at 90 GeV/c^2 in order to avoid possible track mismeasurement problems (see fig. 4.9).

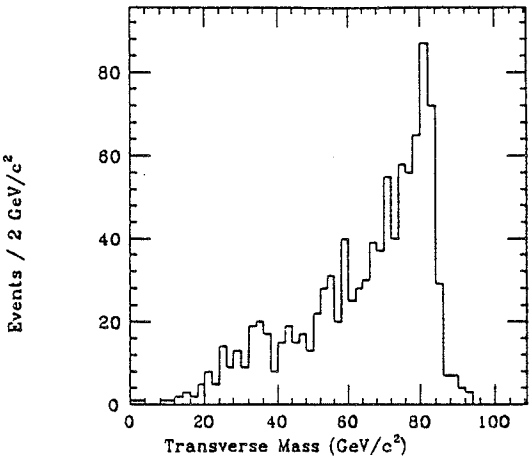

Fig. 4.8 Montecarlo lepton-neutrino transverse mass distribution

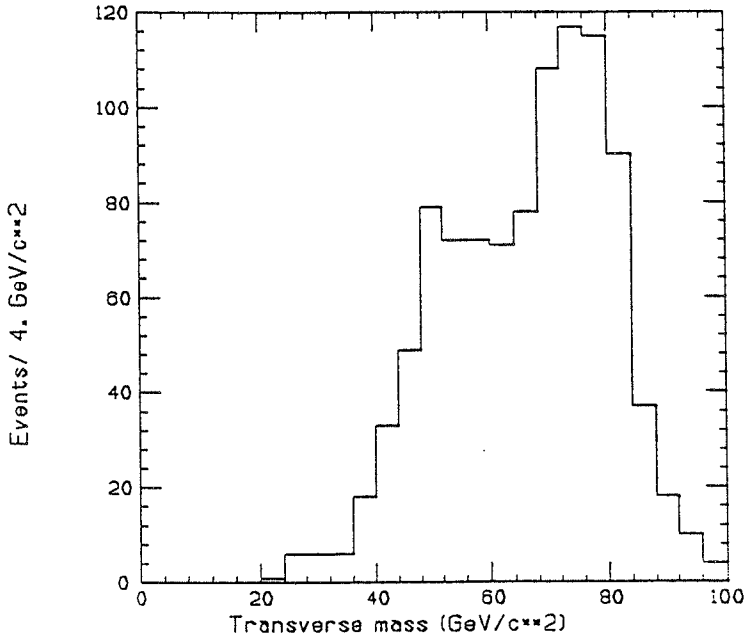

Fig. 4.9 Transverse mass distribution of the W sample.

4.3.6 Pt(W) distribution and Et(Jet) cut.

We also reject events containing a jet with Et (jet) > 10 GeV. This cut reduces the dijet background. It also is a bias against high Pt W's. We applied the cut on Et(Jet) instead of a cut on Pt(W) in order to be in agreement with the other CDF electro-weak analysis. This cut allows us to avoid possible problems with the simulation of high-Pt W's. In fig. 4.10 we show the Pt(W) distribution of our data sample, before and after applying the Et(Jet) cut.

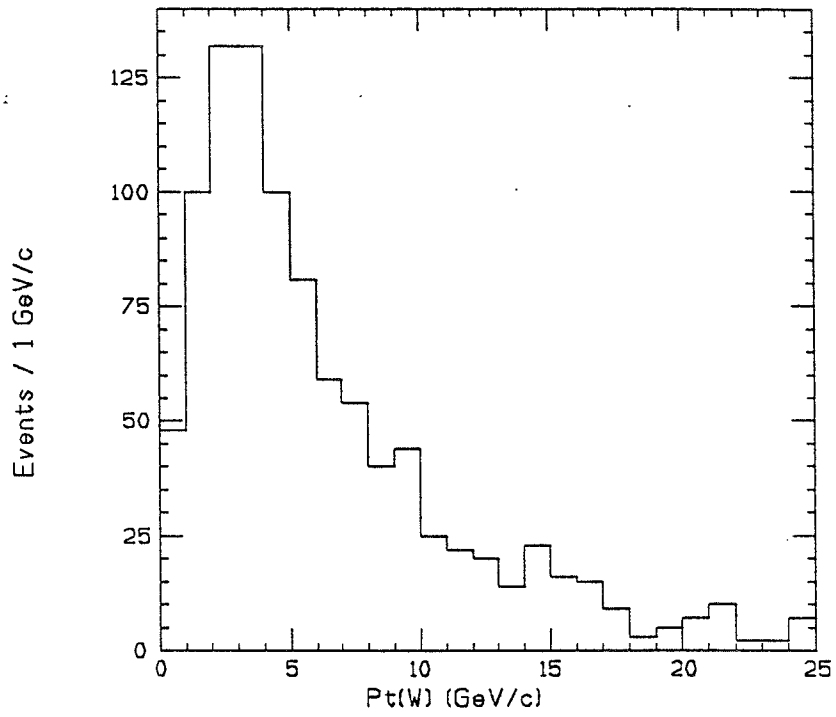

Fig. 4.10 a) Pt(W) distribution, before applying the Et(Jet) cut

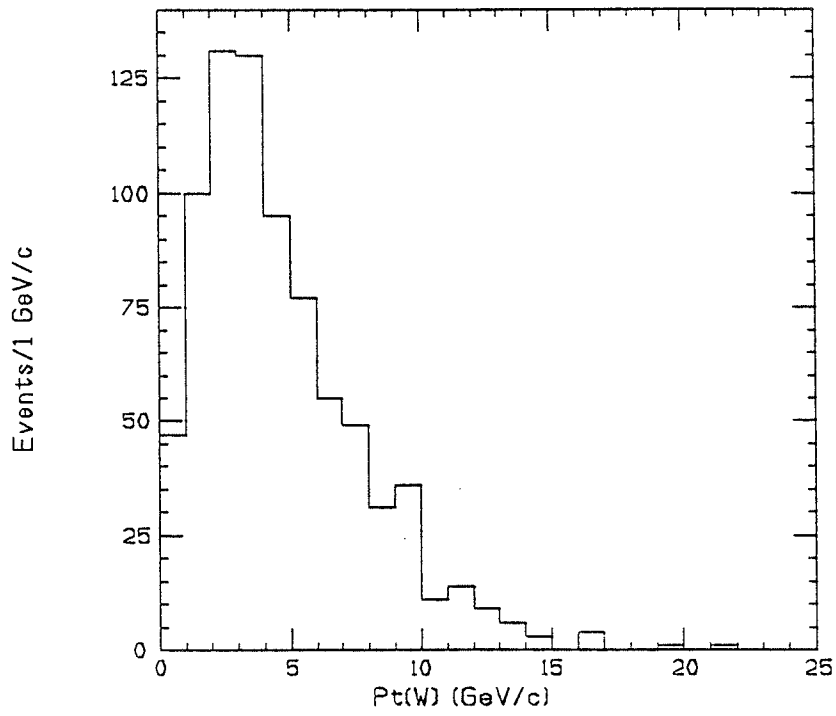

Fig. 4.10 b) Pt(W) distribution, after applying the Et(Jet) cut.

4.4 Background calculations.

After applying our analysis cuts 800 events are left and are dominated by W --> μ ν events. Remaining background sources which need to be analysed are:

- Z events where one of the charged leptons is lost.
- W --> τ ν —> μ ν ν
- Semileptonic heavy-flavor decay.
- technical background as discussed in 4.2.2.

The cuts on Pt(muon), isolation variables, matching variables, transverse mass, the cosmic ray filter, should have considerably reduced all backgrounds. We calculate the remaining contamination for each source of background and its contribution to the total asymmetry.

$W \rightarrow \tau \nu$

The background from W --> τ ν decays followed by τ —> e (or μ) ν ν is estimated from Montecarlo studies to be 3. % of our sample . These events have almost the same asymmetry as the signal, except that they are reconstructed with a wrong transverse mass. It turns out that the relative rate of production and V - A asymmetry is a function of the transverse mass, so this effect could introduce some bias in our measurement. We found from Montecarlo studies that the residual W--> τ ν —> μ ν ν events in our sample may increase the asymmetry at most by 0.03 %.

Non identified Z's

In order to reduce the background due to mis-identified Z^o in which one lepton is not detected, we required that there should not be a second track with Pt > 15 GeV/c in the CTC or in the forward detector. Because the track finding in the forward detector is not 100 % efficient there still could be non-identified Z^o's in our sample. This was investigated using a Montecarlo program which was already used and tested for other kinds of Z analysis. The central muon rapidity distribution of these mis-identified events is shown in fig. 4.11.

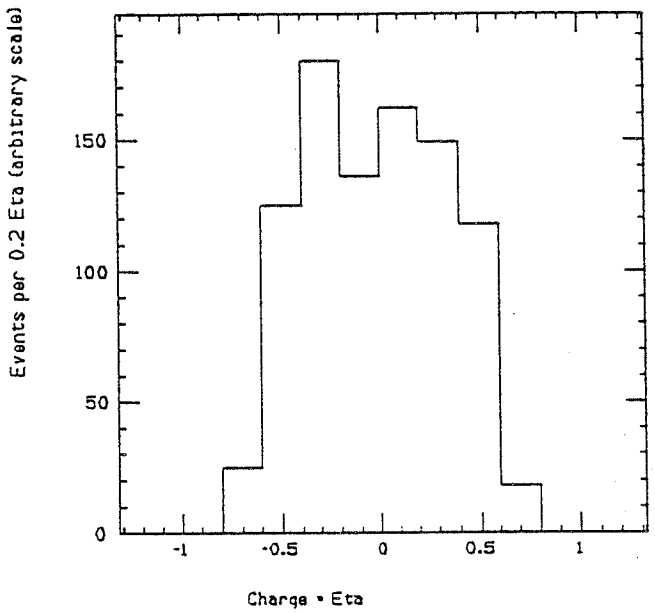

Fig. 4.11 q x η distribution of muons from non-identified Z's (Montecarlo).

We found that our W sample should still contain (30 ± 10) $Z^0 \rightarrow \mu^+\mu^-$ events, where only one central muon is identified. The charge asymmetry found in these events is very small, they therefore tend to decrease the observed asymmetry in the data. We subtracted bin by bin their expected contribution to the observed muon [rapidity x charge] distribution. The uncertainty of 10 events in the prediction for non-identified $Z^0 \rightarrow \mu\mu$ results in an uncertainty on the asymmetry of ± 0.2 % at maximum.

QCD background.

The background from semileptonic heavy flavor decays, decay in flight and punch-through occurs in or near jets. It is plausible that the energy deposition in the vicinity of the muon should look different for background events, when compared to real W's. In W events the muon is well isolated. In addition, real W's cause the presence of a significant amount of missing Et (where the missing Et from the calorimeter has been derived after including the muon Pt), whereas background from all the QCD related processes should show little missing transverse energy. We combine the two variables $\vec{E}_t^{cal}$ and $\sum \vec{E}_t^{R=0.7}$ to a new variable which we call W_{P_t} :

$$W_{Pt} = \vec{n} \cdot (\vec{E}_t^{cal} - \sum \vec{E}_t^{R=0.7})$$

where $\vec{E}_t^{cal}$ is the sum of the calorimeter Et, not corrected for the muon momentum, $\sum \vec{E}_t^{R=0.7}$ is the transverse energy in a cone of R=0.7 around the muon and $\vec{n}$ is a unit vector in the direction of the transverse muon momentum.
Real W events do not cause large missing energy in the calorimeter because muon and neutrino tend to cancel each other. Therefore W_{P_t} is close to 0 or negative for good W events. This is also true for high P_t W's. For not W events the missing energy is caused by the muon mostly and therefore W_{P_t} tends to be positive. We can measure the background by comparing the fraction of isolated over non-isolated muon events at different values of W_{P_t} .
Therefore we study the ratio:

$$\frac{\text{\# of events with Et(in a cone of R=0.4) > 4.0 Gev}}{\text{\# total events}}$$

as a function of the W_{P_t}.

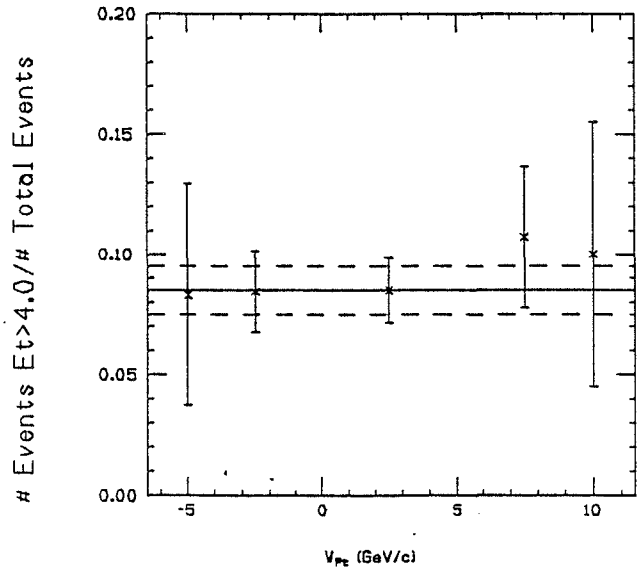

Fig. 4.12 Background estimation.

It was shown that (ref. 28) this ratio is constant for good W events. In fig. 4.12 we plot it for the events passing our standard cuts but not applying the isolation cut. There is no indication for background. We take the two last points to get an upper limit of the background. This gives us a total number of (5 ± 6) background events in our sample, without having applied the isolation cut. We take this number as a conservative upper limit on the number of background events. It corresponds to (0.7 ± 0.7) % background in our final sample.

In order to investigate whether the QCD related background contributes to the asymmetry, we selected a muon sample requiring:

$$\sum E_t^{(0.7)} > 10 \text{ GeV}$$

which is dominated by background. In fig. 4.13 we show the $q \times \eta$ distribution for positive and negative muons [13]. These distributions look almost flat. They show a small total asymmetry of (3 ± 2) %. The effect of this source of background is to dilute any observed asymmetry. We conclude that the influence of a residual QCD background in our sample on the muon asymmetry is negligibly small.

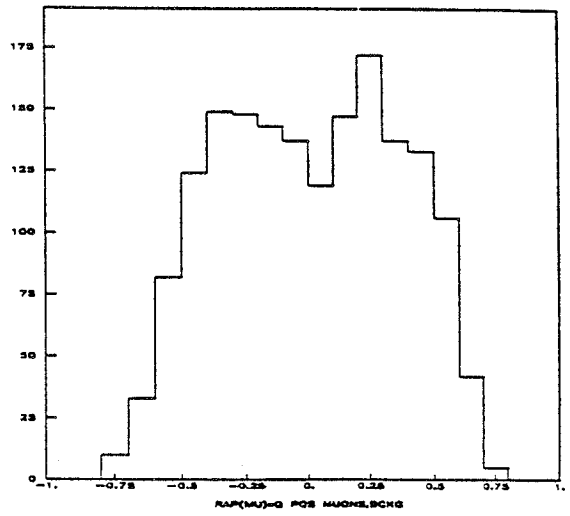

Fig. 4.13 a) $q \times \eta$ of non-isolated positive muons

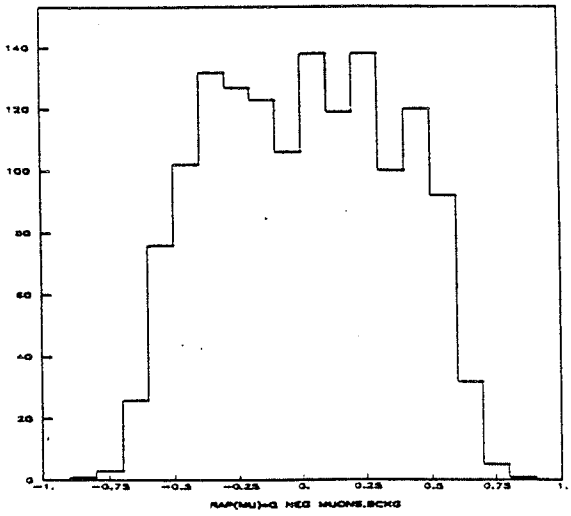

Fig. 4.13 b) $q \times \eta$ of non-isolated negative muons.

Chapter V

Efficiency studies.

The observed asymmetry can directly be compared to theory only if the lepton finding efficiency is charge independent at a given rapidity. Therefore careful studies for possible charge dependencies of this efficiency need to be done [29].

5.1 Muon trigger.

The central muon trigger requires a high pt track pointing at the muon chambers. The association of a CTC track to a CMU stub might be done wrongly at the trigger level, in a way which might introduce charge dependent effects. We investigated possible charge dependent inefficiencies in the CDF central muon sample, due to problems in the muon trigger. For this investigation we used the CDF inclusive muon sample. We selected events requiring one and only one muon candidate by applying the following cuts:

- Pt(muon) > 20 GeV/c
- $|\Delta x| < 3$ cm
- $|\Delta \text{xslope}| < 0.04$ rad
- E(had) in the traversed tower < 8 GeV.

We compared positive and negative muons at positive and negative rapidities. We found 10 events which didn't fire the muon trigger. These events show a positive charge asymmetry of (20 ± 30) %. In our analysis we investigate events which did fire a muon trigger, so events of that type would be missing. They would induce a negative asymmetry. In order to find the trigger efficiency, we studied events with one muon candidate only, obtained with a trigger different from the single muon trigger in which a "golden" muon was reconstructed. These events could have a muon trigger, but we did not require it. We found a total of 160 events. Among these events, 5 did not fire the single muon trigger. This results in a muon trigger inefficiency of (3.1 ± 1.5) %. Combining these two numbers, we obtain a possible error on the asymmetry measurement, due to trigger problems:

$$E = (-20 \pm 30)\% \times (3.1 \pm 1.5)\% = (-0.6 \pm 1.2)\%$$

5.2 CTC track finding.

Due to software or hardware problems, there could be a charge dependence in the CTC track finding process which could introduce some bias in the asymmetry measurement. For the study of this possible effect a sample of cosmic-ray data has been used. This sample has been collected during two special running periods in January and June 1989 using appropriate trigger requirements, because cosmic-ray events have a different timing than $p\bar{p}$

data. One single cosmic ray passing straight through the detector is reconstructed offline as two independent opposite-sign tracks, each with its own characteristics (Pt, ϕ etc.). Since in reality both tracks are the same particle, a perfect detector and reconstruction would give the same parameters, but opposite charge, for each track. One can look for possible charge dependent reconstruction and track finding problems by comparing the parameters of the two reconstructed tracks.

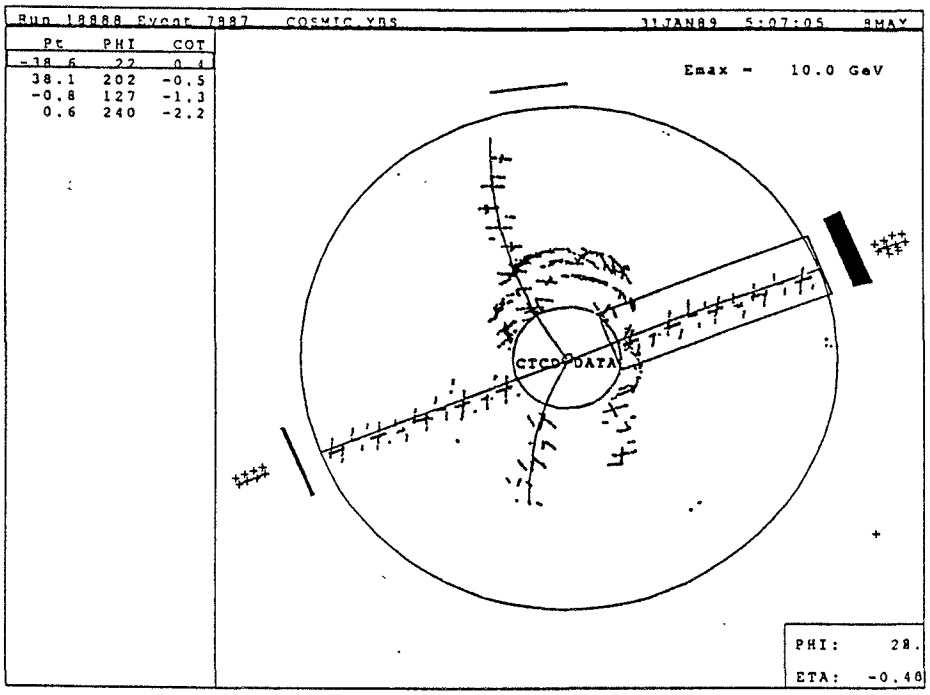

Fig. 5.1 a) End view of the CDF central detector for a cosmic ray event.

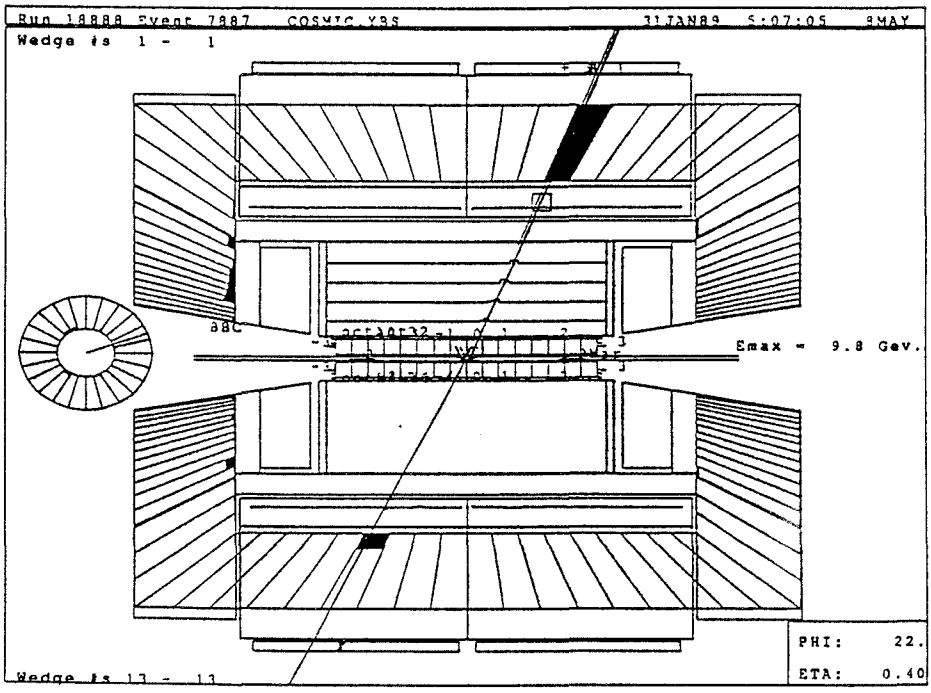

Fig. 5.1 b) Side view of the CDF detector for a cosmic ray event.

In order to study cases where tracks were not reconstructed by the tracking code, we looked at cosmic events where only one of the two segments in the CTC was reconstructed properly. We found 3807 events which had two reconstructed CTC tracks, (a total of 7614 tracks), and 249 events where only one CTC track was found. Studying accurately these events, it results that most of the not found tracks were legitimate misses, because the track went out of the CTC acceptance, exiting the CTC before going all the way throught it radially. Only 11 events appear to be tracking failures. In fig. 5.2 we show one of these events, from the CDF display. 7 out of the 11 tracks had positive charge, 3 had negative charge and one track had 'infinite' momentum. From these numbers we get a possible error on the charge asymmetry due to possible charge dependent track finding inefficiency of at most:

$$E = (0.05 \pm 0.04) \% .$$

With respect to a possible inefficiency in the q(muon) x η(muon) distribution, this of course is a conservative number, because this uncertainty applies to the overall average asymmetry.

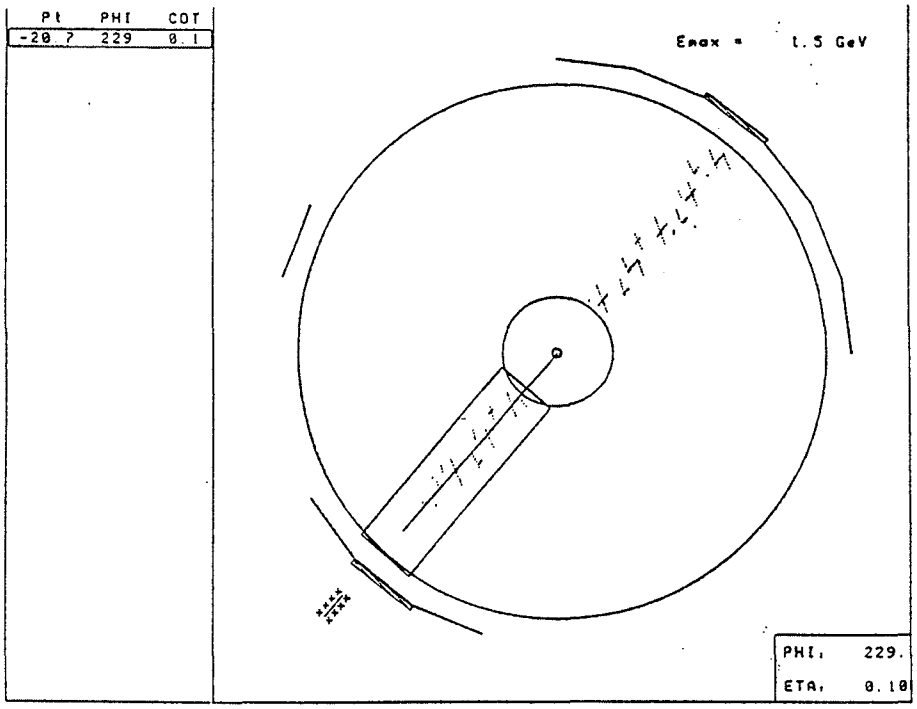

Fig. 5.2 Cosmic event with only one reconstructed segment.

5.3 CTC track reconstruction

The azimuthal wire planes defining the drift cells in the CTC superlayers are inclined relative to the radial direction, in order to compensate for the Lorentz drift angle in the magnetic field (see chapter 2.2.1). In principle this could induce a charge dependent reconstruction efficiency. The study of the offline track momentum reconstruction for positive and negative tracks has been done by tracking experts as part of the Z^0 analysis. Cosmic ray events have been used, providing a sample of positive and negative dimuons of

identical momenta. In samples which were large compared to our W sample, excellent agreement between positive and negative tracks has been found.

Fig. 5.3 shows the distribution of the difference between the curvatures of the two cosmic ray track segments measured in the central chamber [30]. Since it is the same track, but showing opposite curvature in the two segments, the sum should be zero. The difference is normalized to the expected curvature uncertainty expected. If there are no systematic shifts, the distribution would have a mean at 0 and a sigma of 1. The superimposed curve is not a fit, but a gaussian of mean 0 and sigma 1. The agreement is very good. This shows that the chamber is very well aligned.

For our analysis, the possible error on the momentum measurement affects only muons with momentum close to the cut we apply (20 GeV/c). The single track momentum resolution at 20 GeV is $\approx$ 0.4 GeV/c. In a range of about half a GeV/c around our cut on Pt, there are only a few events. Furthermore, there is no evidence for a predominance of a given charge sign. As a cross check of the precision with which we measure the track momentum, we can also refer to the measured mass values of Z^0's, J / psi and Y. The masses of these particles are found to agree to their known values to within one per mille. Also the width of these distributions is consistent with the expected resolution of the CTC [31,32].

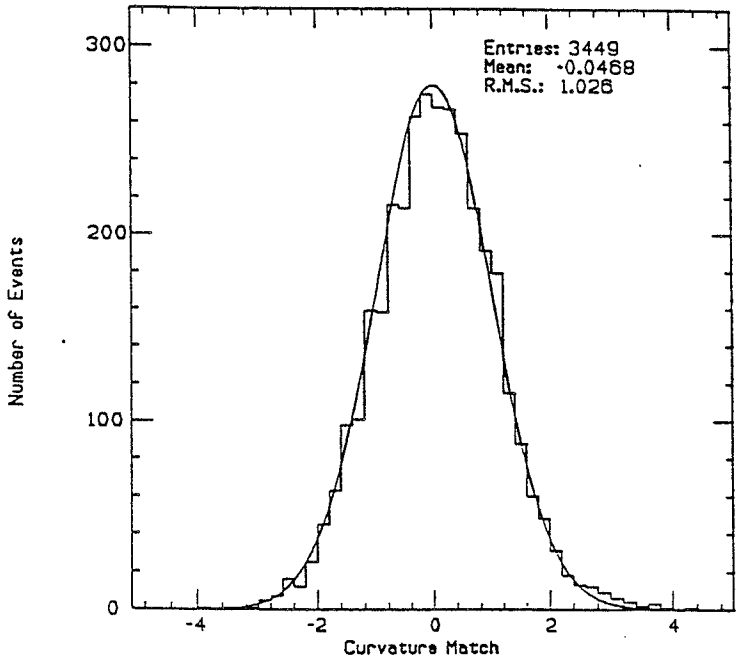

Fig. 5.3 Curvature match between the two tracks in cosmic-ray events.

5.4 CTC - CMU extrapolation.

Due to alignment or software problems, the matching between the CTC track extrapolation into the muon chamber and the muon stub could have a charge dependent bias. In order to study this possible effect, we selected a sample of W's, applying tight quality cuts, but with no matching requirements:

- 0.5 GeV < Σ E_t (ΔR < 0.7) < 5.GeV

- 20 GeV/c < Pt(muon) < 60 GeV/c

- Z (vertex) < 60 cm

- 50 GeV/c^2 < M_t (muon-neutrino) < 90 GeV/c^2

- No additional track with Pt > 15 GeV/c

We got 443 positive muons and 441 negative muons.
The cuts we want to apply on the matching variables defined in Chapter IV are $\Delta x = 2.5$ cm and $\Delta z = 5.$ cm. We plotted the Δx and Δz distributions for positive and negative muons. We want to investigate whether there is a possible charge dependent offset in these distributions. The matching variables distributions are identical within a statistical uncertainty of one bin which corresponds to 0.25 cm in Δx and 0.5 cm in Δz. We investigated how many positive and negative events would pass or not pass the matching cuts when shifting the distributions by one bin. We found that a possible systematic shift by one bin in the matching distributions can introduce an error on the asymmetry due to a charge dependent matching of

$$E = \pm 0.2 \ \% .$$

We assume this as our possible error. With respect to the q(muon) x η(muon) distribution this is again a conservative limit, because it assumes that such an inefficiency would occur only at either positive or negative rapidities. We found that the Δx distributions for positive and negative rapidities are the same within statistics. The Δz distributions for positive and negative rapidities seem to be different by one bin. They are however the same for different charges, at the same rapidity.

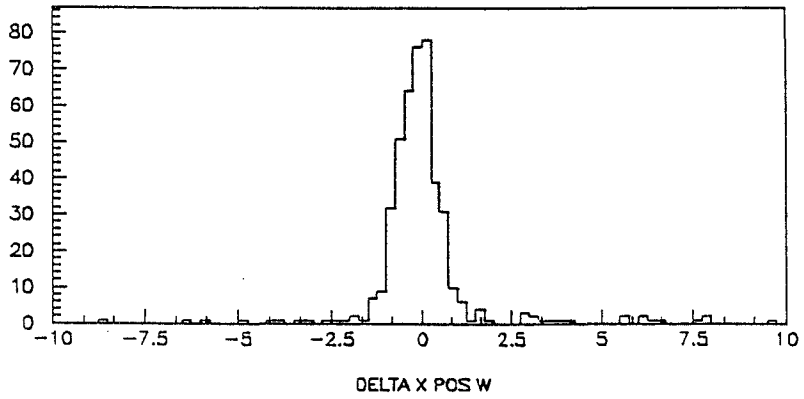

Fig. 5.4 a) Δ x, Positive muons

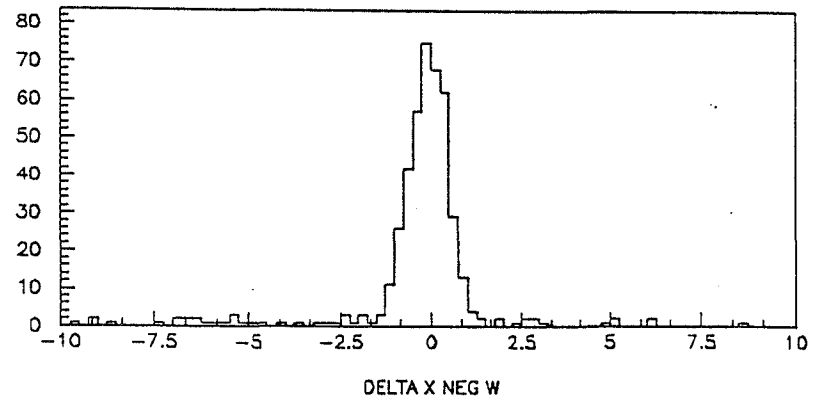

Fig. 5.4 b) Δ x, Negative muons

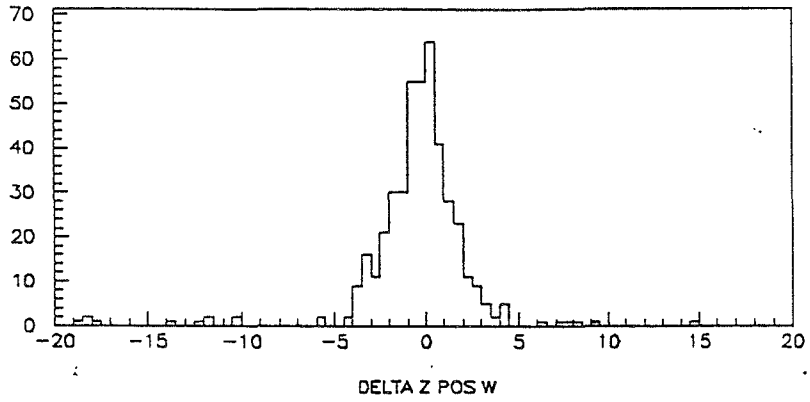

Fig. 5.5 a) Δ z, Positive muons.

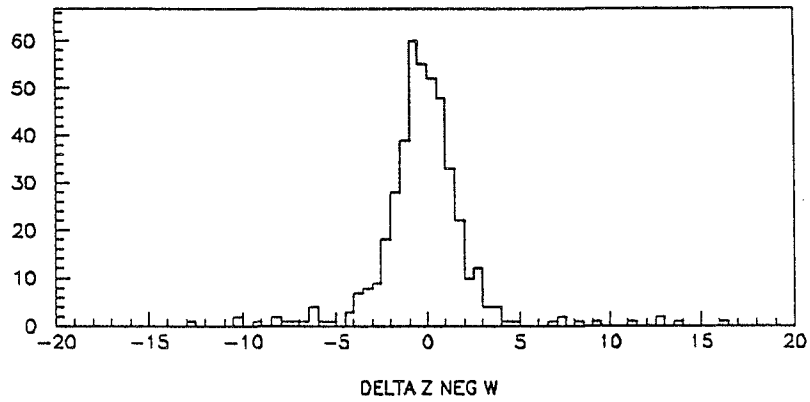

Fig. 5.5 b) Δ z, Negative muons.

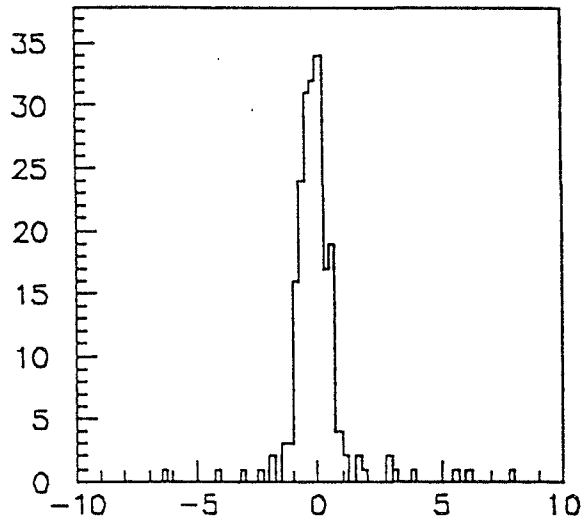

Fig. 5.6 a, Δ x, μ^+, $\eta < 0$.

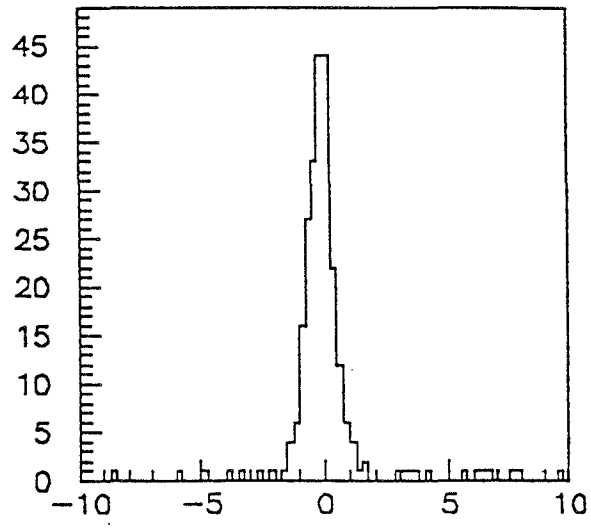

Fig. 5.6 b, Δ x, μ^+, $\eta > 0$.

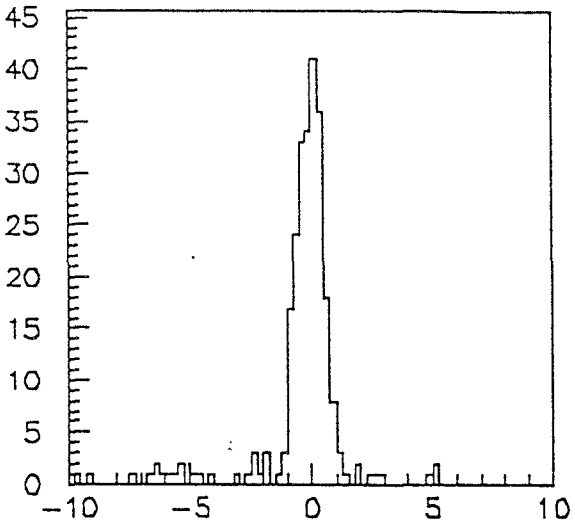

Fig. 5.6 c, Δ x, μ^-, $\eta < 0$.

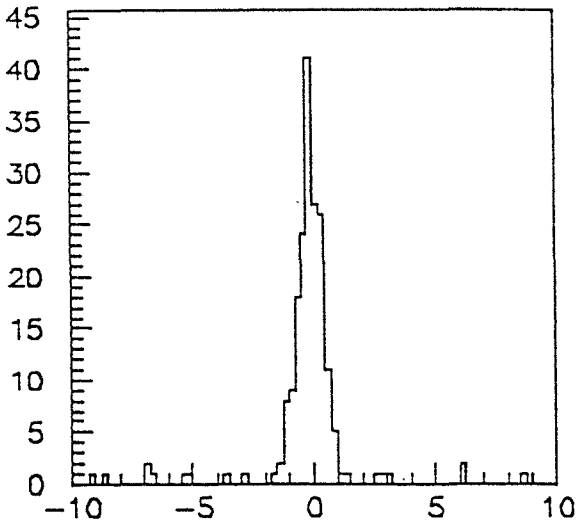

Fig. 5.6 d, Δ x, μ^-, $\eta > 0$.

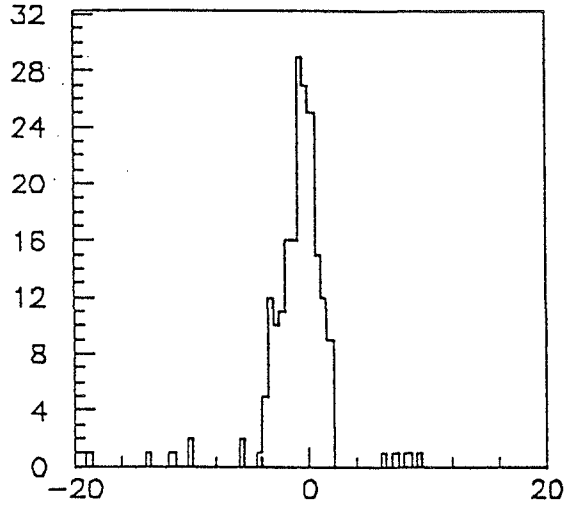

Fig. 5.7 a, Δ z, μ^+, $\eta < 0$.

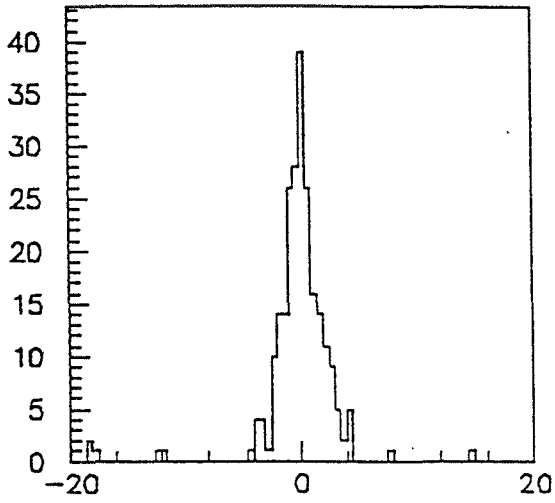

Fig. 5.7 b, Δ z, μ^+, $\eta > 0$.

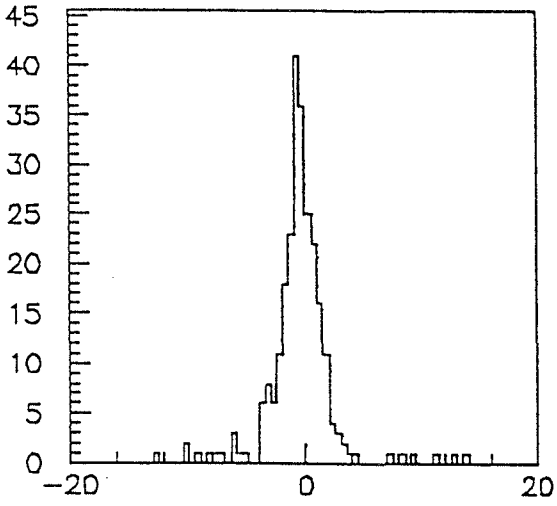

Fig. 5.7 c, Δ z, μ^-, $\eta < 0$.

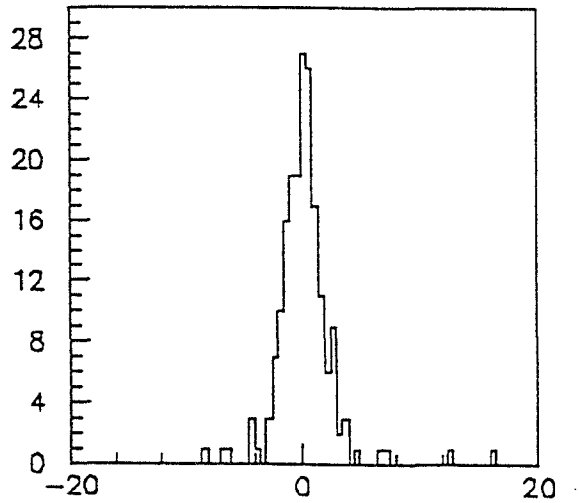

Fig. 5.7 d, Δ z, μ^- , $\eta > 0$.

5.4 Muon stub reconstruction.

We investigated whether the finding of a stub in the muon chambers is charge independent. We used again a sample of cosmic-ray muons requiring Pt > 10 GeV/c. We found 2046 positive tracks which are associated to a muon stub and 2018 negative ones. The difference is within one standard deviation. We studied these events at positive and negative rapidity. They show a positive charge asymmetry (as defined in Chapter I, 4.4) of:

$$E = (0.93 \pm 1.57) \%.$$

Since a perfect detector should not give this asymmetry, we consider this number as the error introduced in our asymmetry measurement because of a possible charge dependent inefficiency in the stub finding process. One can see that the systematic uncertainty which we introduce with this procedure is the biggest one, compared to all those coming from the other efficiency studies we did. It is determined by the size of the cosmic ray sample we used. We will take this error into account in order to arrive to our final conclusion. We need to mention however that we cannot think about any technical reason why the finding of a muon stub should be correlated to the charge of the muon. In future analysis with reduced statistical fluctuations, this systematic uncertainty is likely to be reduced accordingly.

As a general check we studied the matching and Pt distributions for positive and negative cosmic ray tracks, and observed that they have the same shape. We show these distributions in figs. 5.8 , 5.9 and 5.10.

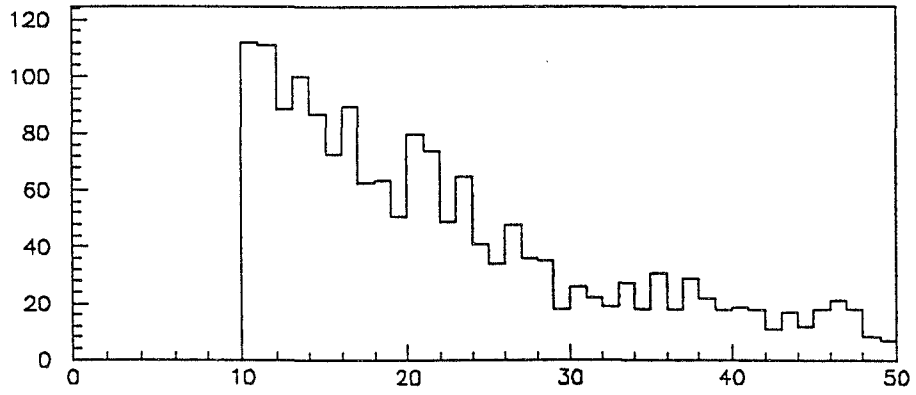

Fig. 5.8 a), Pt spectrum positive events (GeV/c).

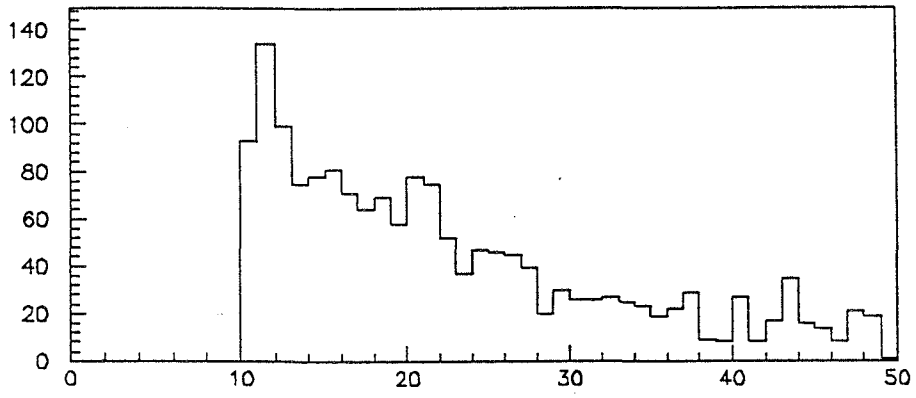

Fig. 5.8 b), Pt spectrum negative events (GeV/c).

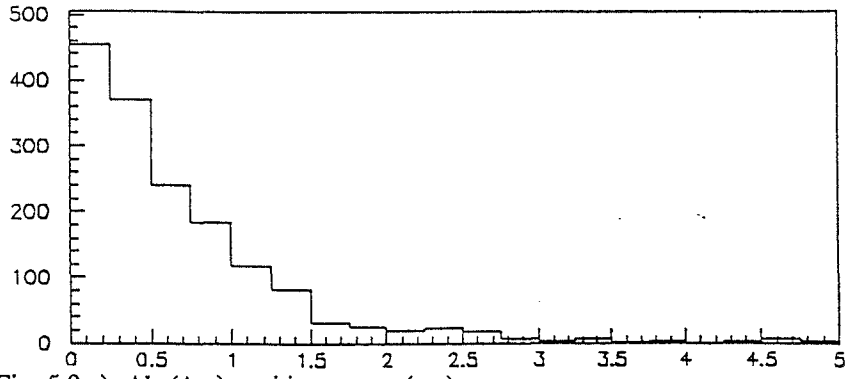

Fig. 5.9 a), Abs(Δ x) positive events (cm).

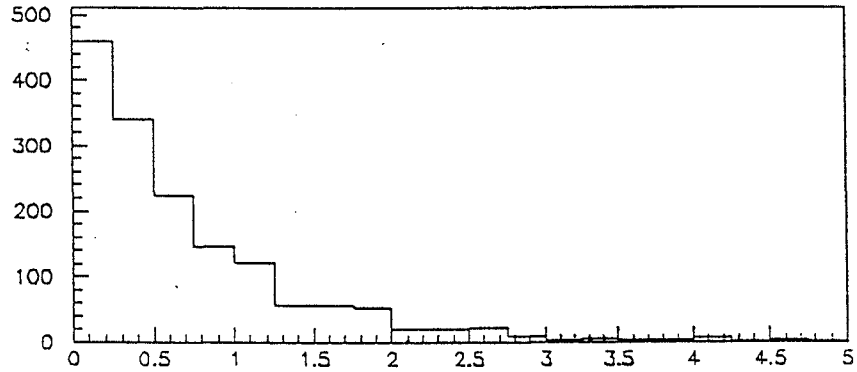

Fig. 5.9 b), Abs(Δ x) negative events (cm).

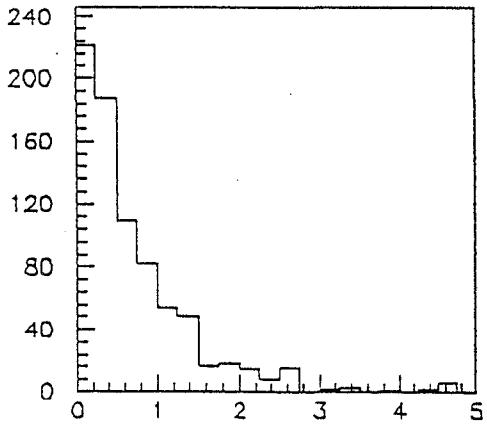

Fig. 5.10 a), Abs(Δ x), positive events, $\eta < 0$.

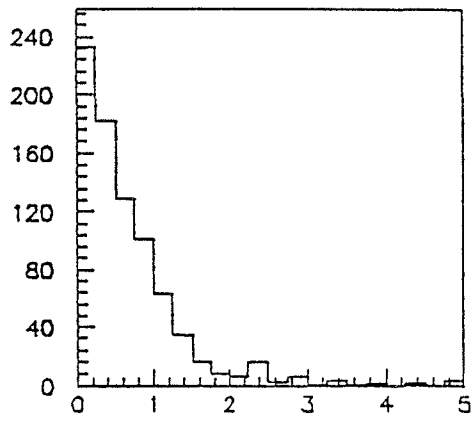

Fig. 5.10 b), Abs(Δ x), positive events, $\eta > 0$.

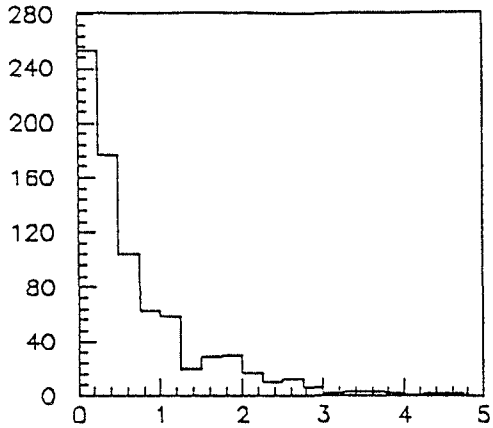

Fig. 5.10 c), Abs(Δ x), negative events, $\eta < 0$.

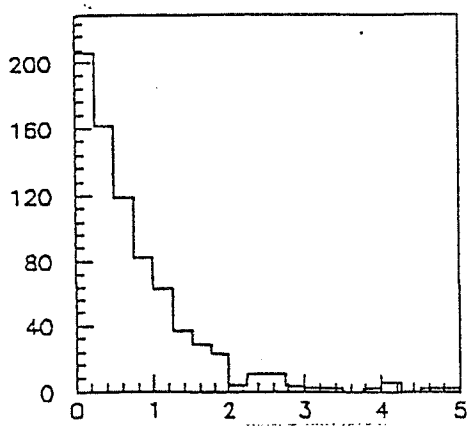

Fig. 5.10 d) Abs(Δ x), negative events, $\eta > 0$.

Chapter VI

Results

6.1 Muon data.

We summarize here all the cuts we used for the central muon W analysis. They have been explained in detail in Chapter IV.

Kinematical cuts:

- Pt(muon) > 20 GeV/c
- No jets with Et > 10 GeV
- 50 GeV/c^2 < Mt (lepton-neutrino) < 90 GeV/c^2

Isolation cuts:

- EM in the muon tower < 2 GeV
- HAD in the muon tower < 5 GeV
- EM + HAD in the muon tower > 0.5 GeV
- ΣE_t ($\Delta R < 0.7$) < 5 GeV

Technical quality cuts:

- $|\Delta x|$ < 2.5 cm
- $|\Delta z|$ < 5 cm

Other requirements:

- Muon trigger.
- Abs(Z) < 60 cm for primary vertex.
- Cosmics and $Z^{o'}$s rejection.

After applying these cuts, we have a sample of:

800 W candidates, (410 W^+ and 390 W^-).

The small excess of positive events is not significant (0.7 sigma). In fig. 6.1 we show the qxη rapidity distribution. Fig. 6.2 shows the transverse mass distribution for our final W data sample. In Table 6.1 we summarize the possible contributions to the asymmetry due to detection problems described in detail in Chapter V. We did not find any charge dependent efficiency within our statistical uncertainty. The test samples used for the study of the systematic uncertainty have high enough statistics to exclude relevant contributions to the asymmetry due to technical problems. In Table 6.2 the corrections to allow for backgrounds and higher order W production diagrams are reported. Since they are so small, these corrections were not applied to our data for the time being (see section 6.4).

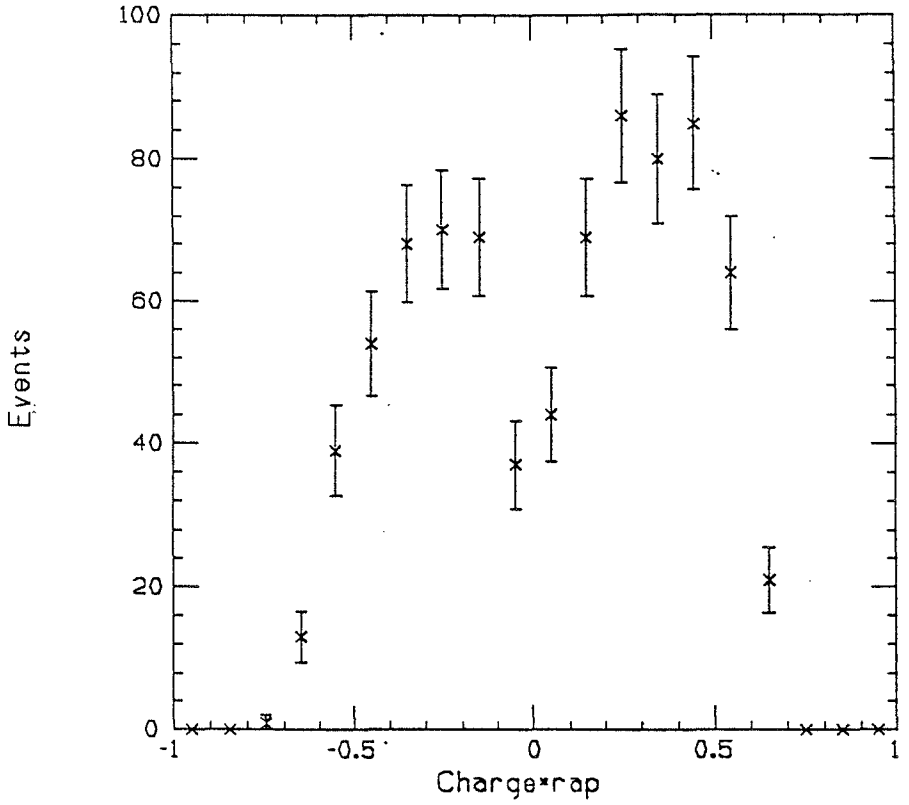

Fig. 6.1 Muon $q \times \eta$ distribution.

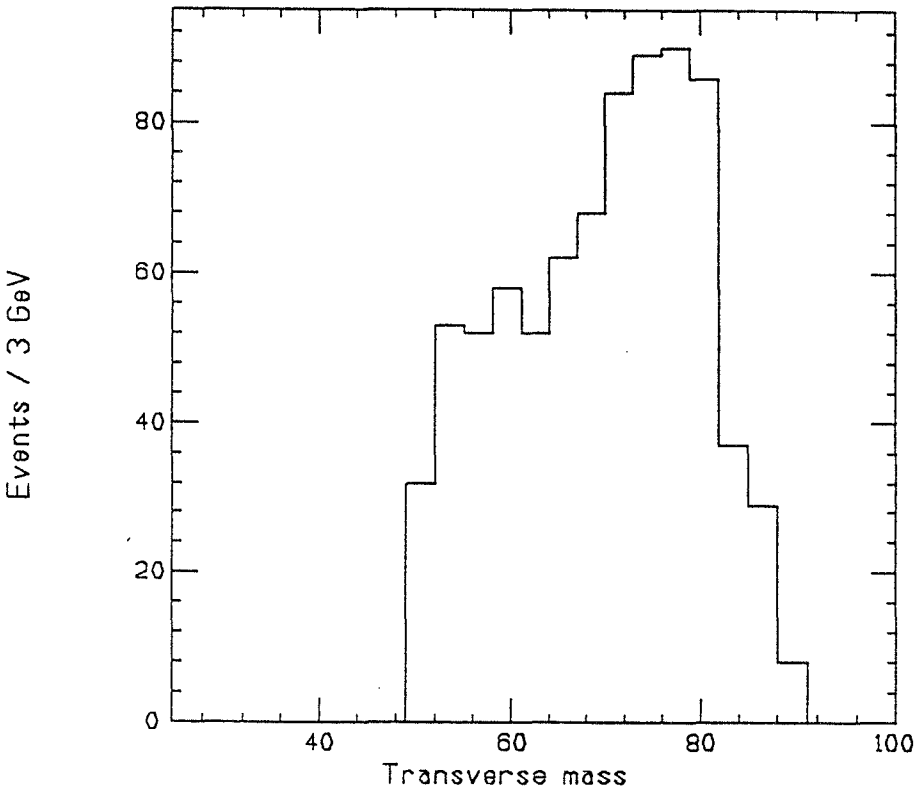

Fig. 6.2 Muon transverse mass distribution (GeV/c^2).

Source of error	Correction to the observed asymmetry
Trigger	(- 0.6 ± 1.2) %
CTC finding	(0.05 ± 0.04) %
Muon stub reconstruction	(0.9 ±1.6) %
CTC-CMU matching	± 0.2 %
	(0.35 ± 2.0) %

Table 6.1

Source of error	Contribution to data	Correction to the observed asymmetry
QCD background	(0.7 ± 0.7) %	+ 0.1 %
Z^o	± 1.3 %	± 0.2 %
Taus	3. %	- 0.03 %
Higher order QCD		+ 0.5 %

Table 6.2

6.2 Electron data.

In parallel to the muon analysis, the central electron data have been used to measure the W asymmetry [13,14]. The study of the asymmetry in the electron channel was mostly done by J.Hauser and S.Ogawa (see ref.14). The cuts used to select high quality central electrons from W decays are:

Kinematical cuts:

- Et (Electron) > 20 GeV
- Missing Et > 20 GeV
- No jets with Et > 10 GeV.
- Transverse electron-neutrino mass > 50 GeV/c^2

Technical cuts:

- Had/Em	< 0.055 + 0.0045*E	(ratio of hadronic to electromagnetic energy).
- Isolation (R=0.4)	< 0.1	(energy around the electron within a cone of radius R=0.4, divided by the electron energy).
- χ^2 (strip)	< 15.	(χ^2 analysis of lateral shower shapes of the CES).
- LSHR	< 0.2	(deviation of energy sharing in towers from that expected.)

Cuts which involve tracking:

- Abs(Dx)	< 1.5 cm
- Abs(DZ)	< 3.0 cm
- E/p	< 1.5

Dx and Dz are the differences between the cluster center measured with CES and an extrapolated track in the ϕ and z directions respectively. E/p is the cluster energy divided by the momentum of the associated track.

Other requirements:

- Abs(Z) < 60 cm for primary vertex.

A total of 1917 events pass these cuts. 923 are W^+ and 994 W^- candidates. The transverse mass distribution and the $q\times\eta$ distribution for electrons are shown in figure 6.3 and 6.4. The possible sources of background are the same previously discussed for the muon channel. We assume that the calorimeter response is charge independent and can introduce no charge asymmetry. Several efficiency studies have been performed in order to find possible charge dependent electron efficiencies. As for muons, all the systematic uncertainties found are small compared to the statistical error of the measurement.In the electron sample there are only very few non-identified Z^0's expected. In table 6.3 we summarize the sources of background, the systematic uncertainties and the corresponding contributions to the asymmetry.

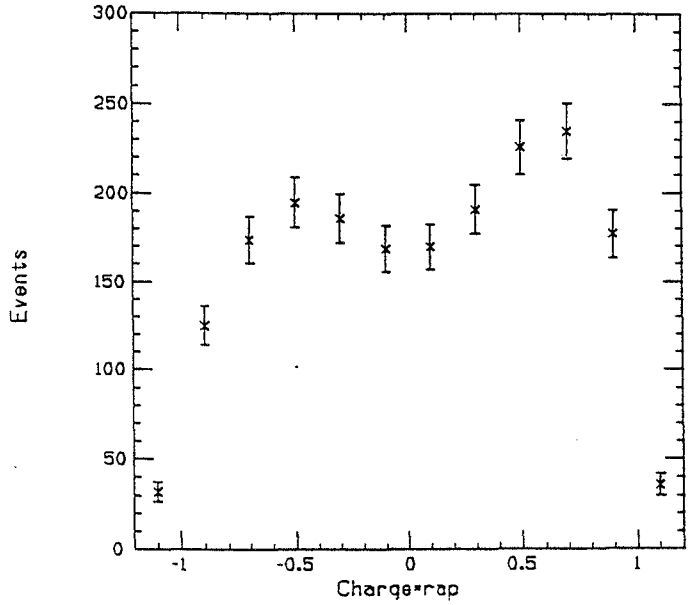

Fig. 6.3 Electron q x η distribution.

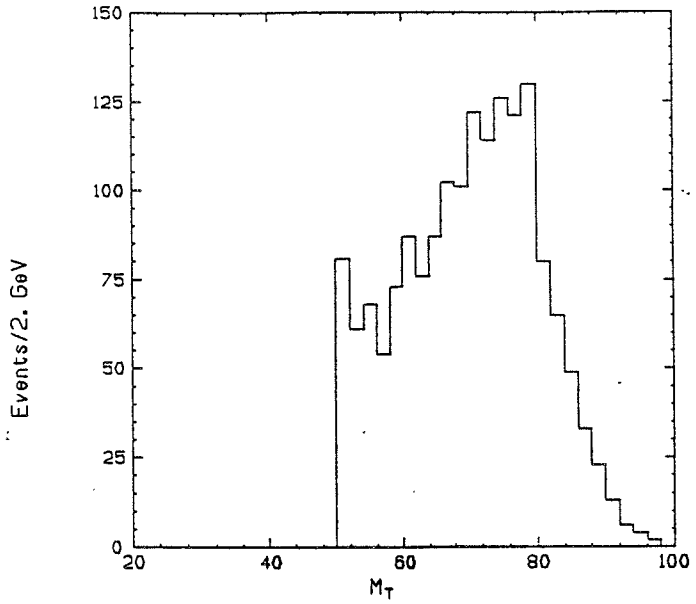

Fig. 6.4 Electron transverse mass distribution (GeV/c^2)

Source of error	Contribution to data	Correction to the observed asymmetry
QCD background	(1.0 ± 0.5) %	+ 0.1 %
Z^o	(0.9 ± 0.3) %	± 0.1 %
Taus	3. %	- 0.03 %
Higher order QCD		+ 0.5 %

Table 6.3 Correction to the asymmetry in the electron channel.

6.3 Statistical error on the asymmetry.

We considered the total number of events N to be binomially distributed between N^+ and N^-. Writing the asymmetry in terms of N and N^+ gives:

$$A = \frac{2N^+ - N}{N} = \frac{2N^+}{N} - 1$$

Thus, using the binomial error on N+

$$\sigma^+ = \sqrt{\frac{N^+(N - N^+)}{N}}$$

the error on the asymmetry is:

$$\sigma_A = \frac{2\sigma_+}{N} = \sqrt{\frac{4N^+(N - N^+)}{N^3}} = \sqrt{\frac{4\,N^+N^-}{N^3}}$$

6.4 Comparison of data with Montecarlo predictions.

In order to be able to compare the results from the muon and the electron channel, we used the same kinematical cuts in both channels. Fig 6.5 shows A as measured from the electron and muon data, together with the theoretical predictions from some structure functions. The theoretical curves are derived for lowest order W production. The different structure functions are labelled in Chapter I, fig.1.8. Here we only remind that the Eichten et al. structure function corresponds to the highest asymmetry, while the Duke-Owens corresponds to the smallest one. The lepton rapidity distribution was obtained by a numerical convolution of the W production matrix element (lowest order) with the parton distributions. We binned the data in intervals of 0.2 in rapidity. One can see that all the predicted curves give values of the asymmetry smaller than the measured ones.

In order to quantify the consistency of the experimental result with the theoretical predictions, χ^2 tests of some existing structure functions were done. The χ^2 function is defined as:

$$\chi^2 = \sum_i \frac{(f(\eta_i) - A(\eta_i))^2}{\sigma_i^2}$$

where $f(\eta_i)$ is the value of the asymmetry in the i-th bin of rapidity, σ_i is the corresponding error and $A(\eta_i)$ is the expected value of the asymmetry in that bin. Smaller values of χ^2 indicate better agreement between data and predictions. Table 6.4 shows the χ^2 of the data with respect to the predictions. In this evaluation the systematic uncertainties and the correction factors are not taken into account. The test prefers the structure functions which predict larger asymmetries.

Structure function	Electrons (6 d.o.f.)	Muons (4 d.o.f.)
EHLQ1	3.6	8.1
EHLQ2	4.9	9.3
DFLM3	5.1	9.3
DFLM2	5.4	9.5
DFLM1	5.7	9.8
MRSB	5.9	10.1
MRSE	6.5	10.7
DO2	13.6	14.8
DO1	16.6	16.1

Table 6.4 χ^2 values data-predictions

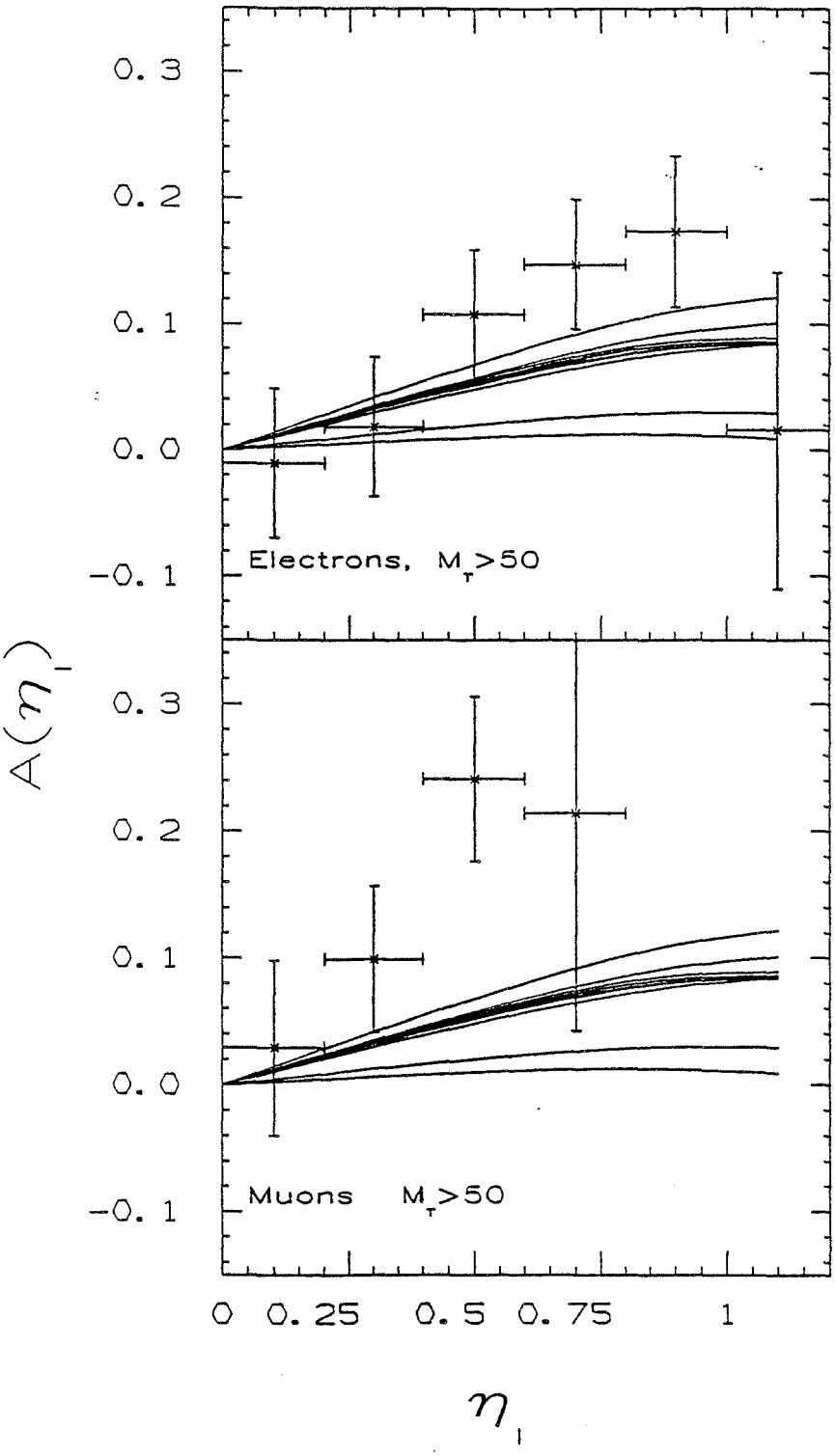

Fig. 6.5 The observed electron and muon asymmetry in W candidate events, compared to asymmetries predicted by various structure functions

The effects of the various possible systematic errors are demonstrated in fig. 6.6, which compares the prediction from EHLQ1 (dotted line) with the data from the muon channel, as in fig. 6.5. We also show the systematic errors on the measured points due to

the uncertainty in the Z^0 events subtraction ($\pm$ 0.2 %). The possible contribution from the 5 ± 6 QCD events is not shown because we consider this number as an upper limit. Subtracting it would shift the measured value by + 0.1 %. The τ contribution could not be seen in the plot because it is too small.

The possible systematic uncertainty due to detection efficiencies is shown as a band of width 2.0 % around the theoretical prediction (see table 6.1). The center of this band is shifted by 0.5 % + 0.35 % (dashed line). The shift of 0.5 % takes the effect of higher order QCD into account (see Chapter III), the shift of 0.35 % accounts for our estimated corrections for systematic errors (see Table 6.1).

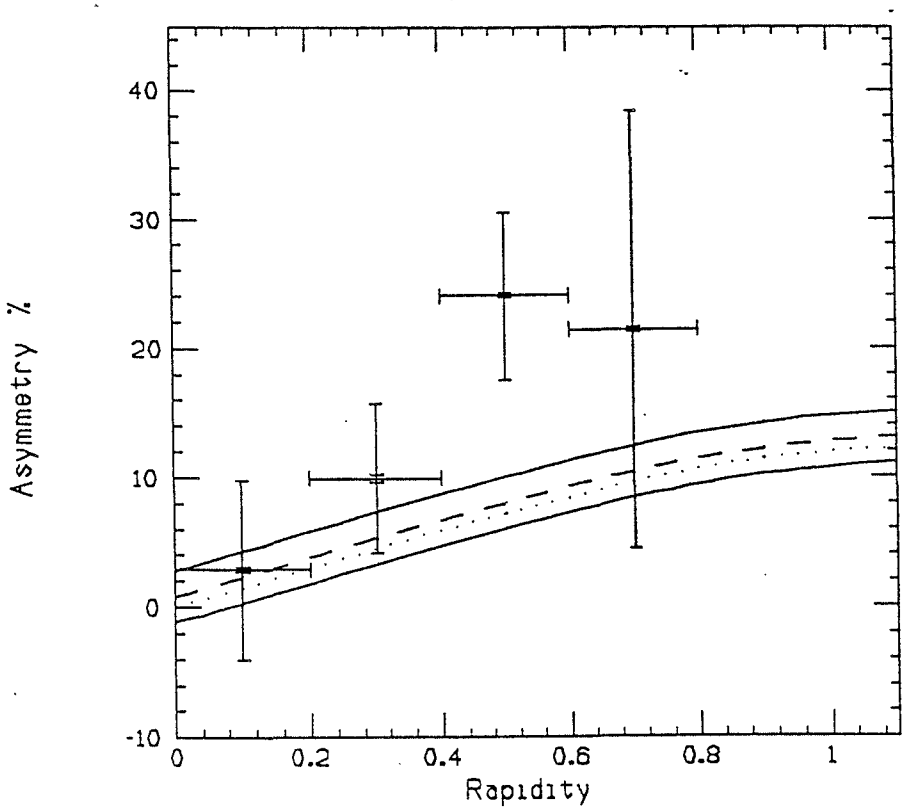

Fig. 6.6 Muon data and systematic uncertainties. Dotted line: Eichten predictions at lowest order. Dashed line: shift of +0.85 % (see text).

Although the systematic errors were estimated very conservatively, the statistical errors on our measurement are still considerably bigger than all the systematic ones. The EHLQ1 structure function appears to match our data best. The DO1 structure function appears to be the least favoured. All the other sets of structure functions are in between, and are not easily distinguisheble one from the other. As an indication of the correctness of our result we note that the measurements in the electron and in the muon channel are in good agreement with each other.

6.5 Future improvements.

At the time being, the precision of our measurement is limited by statistics. Even the estimate of the systematic errors is related to the limited statistics of our test samples and could be improved. Present CDF plans anticipate to collect 20 pb^{-1} of data in the 1991 run. This will allow an improved measurement of the W charge asymmetry, reducing the statistical error by a factor of more than 2. Furthermore, the detector will also be improved and both muons and electrons are expected to be detected with high efficiency also at higher values of rapidity.

Concerning electrons, already now a sample of electron W' s at rapidity of about 1.5, detected in the CDF plug calorimeter, exists and is under study. It consists of 267 events. This sample has already given a very preliminary result for the asymmetry point. The asymmetry measured at $\eta = 1.5$, under the cut $M_t > 60$ GeV/c^2, is A = (15. ± 7.) % (study made by S.Ogawa).

The coverage of the central muon chambers for the next run will be extended up to rapidities of 1.

In the forward region CDF has a muon system which consists of large magnetized steel toroids and drift chamber planes. Due to strong trigger biases, the number of forward W's recorded on tape during the last run is small and it was not possible to use those events for arriving at a meaningful measurement. However, the collected data was sufficient to prove that the detection system works, and the way to select W's has been studied (study made by K.Byrum). We are confident that the next run with a properly turned trigger will yield a large sample of W's from the forward muon system. These muons would allow us to extend our measurement up to rapidities of 3.6.

Conclusions.

Data collected by Collider Detector at Fermilab during the 1988-1989 run have been used to measure the lepton charge asymmetry in $W^{\pm} \rightarrow l^{\pm} \nu$ decay in proton anti-proton collision at $\sqrt{S}$ = 1.8 TeV. This measurement has been used to investigate the W production mechanism and to test proton structure functions in a flavor sensitive way.
From the comparison between data and predictions we conclude that the available statistics is already sufficient to observe that some structure functions are more unlikely. The results in the muon and in the electron channel are in good agreement.
With an increased statistics the developed method could be used for directly giving a parametrization of the parton distribution functions.

References

[1] D.H.Perkins, "Introduction to High Energy Physiscs",(Addison-Wesley Reading, Massachusetts 1987).
I.J.R.Aitchison,A.J.G.Hey, "Gauge theories in Particle Physics", (Adam Higler, Bristol, 1989).

[2] G.P.Yeh, Proceedings of Les Rencontres de Physique de la Vallee d'Aoste, Results and Perspectives in Particles Physics, March 1990 (to be published).

[3] The CDF Collaboration, "A measurement of the W Boson Mass in 1.8 TeV ppbar collisions". Phys. Rev. D (to be published).

[4] R.Field,"Application of perturbative QCD",(Addison-Wesley,1989).

[5] L.B.Okun,"Leptons and quarks",(North Holland,1982).

[6] E.Eichten,I.Hinchcliffe,K.Lane and C.Quigg, "Supercollider Physics", Rev. of Modern Physics,Vol 56,579,(1984).

[7] D.W.Duke and J.F.Owens,"Q^2-dependent Parametrizations of Parton Distribution Functions",Phys.Rev. D 30, 49,(1984).

[8] A.D.Martin,R.G.Roberts, and W.J.Stirling,"Structure-function Analysis and
psi, Jet,W and Z Production: determing the Gluon Distribution",Phys. Rev.D, 37, 1161(1988).

[9] M.Diemoz,F.Ferroni,E.Longo, and G.Martinelli,"Parton Densities from Deep Inelastic Scattering to Hadronic Processes at Super Collider Energies",Z.Phys.C 39,37(1988).

[10] E.L.Berger,F.Halzen,C.S.Kim and S.Willenbrock, "Weak-Boson Production at Fermilab Tevatron Energies", Phys. Rev. D, vol 40, 1989.

[11] C.S.Kim and F.Halzen,"On the Precise Determination of Γ_W/Γ_Z and u/d at Hadron Colliders",MAD/PH/454,(1988)

[12] G.Arnison, et al.,"W Production Properties at the CERN SPS Collider", Lett.Nuovo Cimento,44,1,(1985)

[13] H.Grassmann,S.Leone and T.Westhusing,"Comments on the Rapidity Distributions of Leptons coming from Standard Model W Decay", CDF note 1013.

[14] J.Hauser, M. Miller and S.Ogawa,"Asymmetry in the Central Electron W Sample (a Preliminary Analysis)",CDF note 1110.

[15] The CDF Collaboration,"The CDF Detector: an Overview", Nucl. Instr. and Meth. A271 (1988),387.

[16] R.Snider, et al., "The CDF Vertex Time Projection Chamber System",Nucl.Instr. and Meth. A268(1988),75.

[17] F.Bedeschi, et al.,"Design and Construction of the CDF Central Tracking Chamber",Nucl.Instr. and Meth., A268(1988), 50.

[18] S.Bhadra, et al.,"The Design and Construction of the CDF Central Drift Tube Array", Nucl.Instr. and Meth., A268 (1988) 92.

[19] L.Balka, et al., "The CDF Central Electromagnetic Calorimeter",Nucl.Instr. and Meth., A267 (1988) 272.

[20] S.Bertolucci, et al., "The CDF Central and Endwall Hadron Calorimeter", Nucl.Instr. and Meth., A267 (1988) 301.

[21] Ascoli, et al., "CDF Central Muon Detector", Nucl.Instr. and Meth., A268 (1988).

[22] Marjorie Shapiro and Lina Galtieri, private communications.

[23] H. Grassmann, "W"s as a Tool to investigate Proton Structure Functions", CDF note 1035.

[24] S.Leone, "Lepton and Jet Asymmetries in W+Jet events", CDF note 1091.

[25] T.K.Westhusing,"Observation of W --> μν Decays in Proton-Antiproton Collisions at sqrt(s)= 1.8. TeV", (Ph. D. Thesis, unpublished).
[26] A. Gauthier,"Efficiency of the Level 1 Central Muon Trigger ", CDF note 937
[27] G.Fernow,"Introduction to Experimental Particle Physics",(Cambridge University Press,1986)
[28] T. Westhusing, "A Signal Subtraction Technique to Determine the Number of W-->μν Candidates".CDF note 1113.
[29] H.Grassmann,S.Leone, "Charge Dependence of Muon Detection Efficiencies", CDF note 1130.
[30] A.Gauthier," CTC Tracking Studies with Cosmic Rays",CDF note 965
[31] CDF Collaboration," Measurement of the Mass and Width of the Z^o Boson at the Fermilab Tevatron".Phys.Rev.L. 63,720 (1989)
[32] T.Liss," J/psi and Y Production at CDF".Published in Proceedings of the 8th Topical Workshop on $p\bar{p}$ Collider Physics,Castiglione della Pescaia,1989.